Detailed numerical simulations of primary atomization of airblasted liquid sheet

Anirudh Asuri Mukundan, Thibaut Ménard, Jorge César C Brändle de Motta, Alain Berlemont

Detailed numerical simulations of primary atomization of Airblasted liquid sheet

Anirudh Asuri Mukundan[a,1], Thibaut Ménard[a,b,*], Jorge César Brändle de Motta[a,b], Alain Berlemont[a]

[a] *CNRS UMR6614 CORIA, Saint-Étienne-du-Rouvray, France*
[b] *Université de Rouen Normandie, Saint-Étienne-du-Rouvray, France*

Abstract

This paper investigates the primary atomization of Airblasted liquid sheet through detailed numerical simulations. The atomization of liquid sheet under Airblasting conditions involve complex mechanisms and a thorough understanding is necessary. A planar pre-filming Airblast atomization configuration have been chosen to study the breakup of liquid sheet/film injected on a solid flat pre-filmer plate. We have investigated a single operating point that is directly relevant for efficient liquid fuel atomization for cruising condition of the aircraft. This configuration has been chosen based on an experimental investigation of Gepperth et al [S. Gepperth, A. Müller, R. Koch, H.-J. Bauer, Ligament and droplet characteristics in pre-filming airblast atomization, Proceedings of the ICLASS, 12th Triennial International Conference on Liquid Atomization and Spray Systems, September 2-6, Heidelberg, Germany, 2012] for the Airblast atomization. The numerical simulations have been performed using in-house Navier-Stokes solver that uses consistent mass and momentum flux computation technique. The purpose of this work is to provide a comprehensive database and analyses of the Airblast atomization of liquid sheet that include studies on the effect of velocity profile on the atomization characteristics, detection of occurrence of secondary atomization and drop coalescence, and extraction of near-field atomization characteristics. The qualitative analyses of the results from the simulations showed that there are two major mechanisms of liquid film breakup – sheet/bag breakup and ligament breakup. The drop velocity distribution computed from the simulations was found to be agreeing well with the experimental data while an under-prediction was found for the drop size distribution albeit of the simulations are of same order of magnitude as that of the experiments. Based on the atomized droplet data, both the secondary atomization and drop coalescence have been observed to occur in the simulations. The quantitative analyses of the near-field liquid ligaments results revealed that the lengths of these ligaments are in satisfactory agreement with the experimental data while an under-prediction in the ligament velocity has been observed. Finally, an excellent agreement between simulations and experimental data have been found for the Sauter Mean Diameter (SMD) of the atomized droplets.

Keywords: Primary atomization, Airblast atomization, Incompressible flows, Multiphase flows, Moment of Fluid method, Drop size distribution

1. Motivation and objectives

Air transport has been one of the fastest mode of transportation of passengers and freight between continents in the world. Despite the current COVID-19 pandemic, with the stage-by-stage vaccine roll-out in many countries, it is predicted the aviation industry will soon bounce back to the level of pre-COVID era.

*Corresponding author
Email addresses: anirudh.mukundan@math.ubc.ca, anirudh.mukundan@coria.fr (Anirudh Asuri Mukundan), thibaut.menard@coria.fr (Thibaut Ménard)
[1] current address: Department of Mathematics, University of British Columbia, Vancouver, Canada. *Contact Email address:* anirudh.mukundan@math.ubc.ca

In fact, the pre-COVID estimates [1] have observed that the aviation industry has experienced a growth of about 2.5 times the number of passengers since the year 2000. Furthermore, Airbus [2] had a forecast of a 4.3% air traffic growth for the next 20 years. The Advisory Council for Aeronautics Research in Europe (ACARE) and National Aeronautics Research and Development plan has put forth stringent regulations norms that include the norms on the pollutant emissions such as CO_2, NO_x, and noise reduction. With these regulations data on hand, it is imperative to design aero engines with high efficiency, low fuel consumption, and reduced pollutant emissions.

To that end, the lean combustion technologies (LCT) such as lean premixed prevaporized (LPP) combustion, Moderate or Intense Low-oxygen Dilution (MILD) combustion concepts are commonly employed in the gas turbines. In fact, the LCT is now a standard practice in reaching ultralow pollutant emissions by controlling the combustion temperature [3]. With the LPP concept, low temperature fuel combustion has become possible which thereby reduces the NO_x emissions. Furthermore, with the advent of MILD combustion concept, low temperature combustion in addition to dilution of reactants to reduce both NO_x have become possible in gas turbines. In order to extract the full efficiency from the lean combustion concept (LCC), it is imperative to have high quality of atomization/breakup of the injected liquid fuel. Moreover, this high quality of atomization has to be maintained at all operating conditions of the aircraft even at high altitude where the temperature can drop as low as $-40\,^{\circ}\mathrm{C}$. These objectives are met through a fuel injection technique which involves Airblast atomization of injected liquid fuel. Airblast atomization is the physical process in which low speed liquid fuel stream is sheared by high speed air (i.e., gas) stream thereby leading to breakup into small drops and ligaments. In fact, a planar pre-filming type of Airblast atomization have been employed in the aircraft engines involving a thin film of liquid fuel is injected on a solid flat plate which is then destabilized into ligaments and droplets with the high speed air flowing above and below the plate. Quite often, the mean velocity of the gas is about 100 times larger than that of the liquid which results in an Airblasted-type atomization process for the liquid fuel breakup into droplets. There are numerous breakup mechanisms involved in the pre-filming Airblast atomization process. Hence, in order to control the fuel atomization, an improved understanding of this atomization process is necessary.

Since the introduction of the concept of Airblast atomization by Lefebvre and Miller [4], there have been numerous investigations of two configurations of Airblast atomization – cylindrical and planar configurations. In the former, the liquid and gas are injected in a co-flowing setup in which the destabilization of the liquid jet by the high speed gas causes the atomization into droplets. In the latter, a thin liquid film is injected on a flat plate which is then destabilized into droplets by the high speed gas stream flowing above and below the plate.

On one hand, Lasheras et al. [5], Villermaux [6], Marmottant and Villermaux [7] performed extensive investigations to understand the breakup physics of the cylindrical Airblast atomization configuration. These studies found that the liquid/gas interface is first subjected to Kelvin-Helmholtz (KH) instability due to momentum and velocity difference between the liquid and gas phases. The KH instability results in the surface waves on the liquid/gas interface which then forms bulges on the surface. These bulged portion of the interface are stretched into ligaments due to the high speed co-flowing air due to Rayleigh-Taylor (RT) type instability. These ligaments then subsequently breakup into droplets due to the capillary effect from the Rayleigh-Plateau (RP) instability. Apart from the experimental investigations, there have been attempts to numerically simulate the atomization for this cylindrical configuration. For example, Chiodi et al. [8], Chiodi and Desjardins [9, 10] were able to reproduce the breakup physics through numerical simulations using geometric liquid volume fraction transport method [11] and accurate conservative level set (ACLS) method.

On the other hand, the planar configuration of Airblast atomization has different breakup physics compared to the cylindrical configuration. Hence, there have been many experimental [12, 13, 14, 15] and numerical works [16, 17, 18, 19] that investigated into understanding the breakup physics and the atomization characteristics such as drop size distribution (DSD) and drop velocity distributions (DVD). Many of the past experimental studies have found that the aerodynamic forces play a significant and key role in the droplet sizes; specifically, the increase in the mean air velocities resulted in reduction in the droplet sizes [20, 21, 22, 23] while a reduction in the Sauter Mean Diameter (SMD) has been observed with the increase in the surface tension of the liquid fuel [20, 21]. Multiple works using numerical simulations have been

performed in the past years, for example, Fuster et al. [24] studied the instability frequency of the primary break up of planar coflowing sheets of water and air at dynamic pressure ratios of 0.5 to 32. Recently, Agbaglah et al. [25] studied the destabilization of the air/water planar liquid sheet and found an excellent agreement between experiments and simulations for liquid cone length, spatial growth of primary instability, and maximum wave frequency. The investigations by Bilger and Stewart Cant [17] performed simulations of planar Airblast atomization with a laminar inlet velocity profile for the gas phase and developed a regime diagram for the atomization process using the liquid and gas phase velocities as the abscissa and ordinate, respectively.

Although there have been many numerical studies carried out in the past, they have predominantly focused on an operating condition that are not directly relevant to an aircraft engine operating condition. Since the products of liquid atomization are different for different operating conditions, Gepperth et al. [14] performed experimental investigation of planar pre-filming Airblast configuration using Shellsol D70 (surrogate of Jet A-1 fuel) under various operating conditions. Of these operating conditions, the aircraft altitude relight condition has been of highlighted interest in their work. This operating condition is relevant for the successful relight of the flame within the jet engine during flame blow-off scenarios at high altitude. In fact, their study extracted near-field data about the breakup length and velocity of disintegrating liquid ligaments and far-field atomization characteristics about droplets under various velocity of the gas stream. These characteristics are relevant because the Airblast atomization thrives on the gas phase velocity and the momentum flux ratio ($q = \rho_{\text{liq}} u_{\text{liq}}^2 / \rho_{\text{gas}} u_{\text{gas}}^2$) depend on the velocity of the gas stream. Following this experimental investigation, there have been multiple experimental studies [26, 27, 28] as well as numerical studies that used large eddy simulations (LES) [29, 30, 19] for this configuration; embedded direct numerical simulations (eDNS) [31, 32, 33, 16] in which the DNS have been performed in a small domain embedded inside larger LES domain. Recently, Warncke et al. [16] used a diffused interface VOF method using OpenFOAM framework for simulating the primary atomization of a planar pre-filming Airblast atomizing liquid sheet using eDNS approach. A satisfactory agreement in the results between the simulations and experiments have been found from their study. However, the limitations to the diffused interface method has been profoundly observed in the computation of the statistics of the droplet data. A recent work by Braun et al. [34] used meshless smoothed particle hydrodynamics (SPH) for numerically predicting the air-assisted atomization and compared their results with that from the work of Gepperth et al. [14].

Although there have been several studies in the past that performed the numerical explorations and investigations into Airblast atomization, the effect of inlet velocity profile on the atomization characteristics, droplet breakup mechanisms, and on the ligament breakup lengths and velocities are still missing links. Our work on the investigation of primary breakup of pre-filming Airblast atomization through detailed numerical simulations will provide answers to improve the understanding of these links. Therefore, the objectives in this work are to:

- understand and identify predominant physical breakup mechanisms of Airblast atomization,
- investigate the atomization characteristics such as droplet size and velocity distributions,
- find the presence of secondary atomization and coalescence of droplets in the computational domain,
- find the effect of liquid and gas inlet velocity profile on the atomization characteristics, and
- extract near-field data about ligaments such as breakup lengths and velocities as well as breakup frequency.

To that end, results from the simulations of a practically relevant liquid fuel injection configuration of a primary breakup from a planar pre-filming Airblast atomization process is presented in this paper. Such a type of liquid fuel atomization configuration is employed is aero engines in which a thin film of liquid fuel injected over a solid flat plate is destabilized and disintegrated into droplets by the high speed flowing air. The operating condition is chosen judiciously in such a way that it is practically relevant for engineering application as well as it is not computationally expensive to perform detailed numerical simulations to study liquid fuel breakup physics. The chosen operating condition pertains to aircraft altitude relight condition

in which the reignition of the flame is necessary for the aero engine to deliver the required thrust. Such a condition is not uncommon for the aero engines since the cruising altitude of an aircraft is about 11,000 m ($\approx 36,000$ feet) at which altitude the temperature of the air can go as low as $-50\,^{\circ}$C.

This paper is organized as follows. Section 2 presents the details about the investigations performed by the experiments whose data are compared later with the results from the simulations performed in this work. Furthermore, this section presents the chosen computational domain along with the operating conditions for which the numerical simulations are performed. Then, the configuration, case setup, initial and boundary conditions, and numerical methods for the flow solver are presented in Section 3. Finally, the results from the numerical simulations are presented in Section 4 that include detailed qualitative and quantitative analyses of the breakup mechanisms, atomized droplets, and liquid ligaments.

2. Investigation domain and operating conditions

The simulations for the primary atomization of Airblasted liquid sheet presented in this work are performed for a reduced geometry of an annular aircraft engine combustor similar to the experimental work of Gepperth et al. [14] and numerical work of Warncke et al. [16]. The rationale behind the reduction of the complex combustor geometry is to be able to perform detailed numerical simulations of primary atomization zone at a modest computational cost. The following subsections present the details of the configuration and operating conditions employed in the experimental investigation [14] and the numerical simulations performed in this work.

2.1. Experimental study

The experiments have been conducted at the spray test rig at the Institut für Thermische Strömungsmaschinen (ITS) in the Karlsruher Institut für Technologie (KIT). The test section of the experiment [14] is a two-dimensional abstraction (i.e., reduced geometry) of an annular combustor consisting of four wall segments and pre-filming flat plate upon which the liquid fuel is injected as a thin film/sheet. This film is then destabilized by the high speed air flowing above and below it. The air from the mixer have been split into two streams such that each stream flows above and below the pre-filmer plate. The liquid is continuously fed on the pre-filmer plate through a set of 50 equidistant distributed holes each with a diameter of 0.5 mm. The liquid flow through the test section have been controlled by a mass flow meter/controller.

The primary breakup process and the flow of the liquid film has been obtained through high speed shadowgraphy technique. A set of two high speed video cameras of 7 kHz at a spatial resolution of 13.89 µm with a field of view of approximately 14.2 mm × 14.2 mm have been used. The cameras have been placed at a 90˚ shift so that both the side and the top view of the film disintegration can be captured. The exposure time has been reduced to 1 µs minimizing the blurring effect of the fast deforming liquid structures and droplets. The measurement volume have been illuminated using two 500 W halogen spotlights mounted opposite to the cameras. Then, a double image (each shifted spatially by 90˚) has been recorded every 3 s over a total time of 30 s with the rationale that each recorded droplet must have left the field of view within 3 s. Each drop found in the double image has been considered for the purpose of statistical analysis such as computation of probability density function (PDF) of drop size distribution (DSD) and drop velocity distribution (DVD). In addition to the far-field droplets, the near-field liquid ligaments are captured from the shadowgraphy images from the accumulated liquid in the trailing edge of the pre-filmer plate as shown in Figure 1. The technique of ligament tracking velocimetry [35], has been employed to distinguish and separate the droplet liquid structure and ligament liquid structure in the images. This technique is based on on back light illumination (i.e., shadowgraphy) with a double-pulsed laser. The field of view is 12 mm × 16 mm with a spatial resolution of 10 µm. The main advantage of this measurement technique is that the details about the droplets and the accumulated liquid shown in Figure 1 are obtained simultaneously. A total of 38,000 droplets and 13,000 liquid ligaments have been recorded from the shadowgraphy images.

Robust statistical results have been derived from the obtained experimental images using an efficient algorithm [36] which has been extended by a depth of field (DoF) correction to further increase the measurement accuracy. It is to be remarked that, within the context of this algorithm, the droplets need not

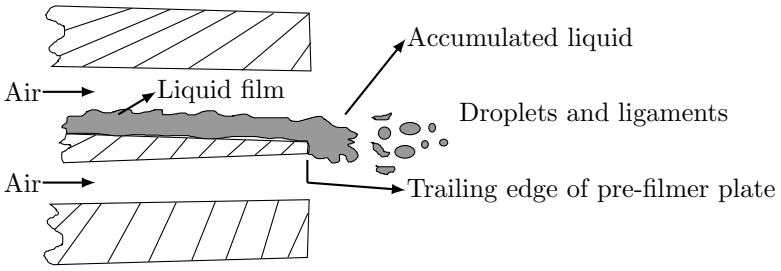

Figure 1: Illustration of instability waves on liquid film, liquid accumulation at pre-filmer plate edge, as well as droplet and ligament formation.

be spherical to be able to measure its diameter and velocity. The post-processing algorithm for the images developed at the ITS [37, 36, 38] can be divided into four parts. First, a gray scale image is obtained from each experimental raw image using a threshold value based on pixel intensity distribution. Second, connected structures are identified using a contour tracking algorithm which further divides the area into droplets and accumulated liquid (from which the liquid ligaments are disintegrated). Third, droplet velocity is computed using a velocity estimated from the particle image velocimetry (PIV) as a "first guess" using which the final velocity is computed using the droplet displacement between consecutive frames and the time gap between these frames for each droplets. And, finally, geometrical parameters of the accumulated liquid such as length and velocity of liquid ligaments are computed.

The uncertainties in the experimental measurements quantified using the method of Kline and McClintock [39]. These uncertainty values are measured to be 3% for air velocity, 0.5% for liquid mass flow, 4% for measurement of drop size and velocity summing upto a an approximate 7%. For more detailed information about the experimental setup and post-processing procedure, the reader is referred to Refs. [37, 35, 14, 36, 16].

2.2. Numerical simulations

A planar pre-filming configuration is considered in this work for detailed numerical simulations of primary atomization of Airblasted liquid sheet. This configuration, as shown in Figure 2, is a geometry simplification of the annular atomizer. In this simplified geometry, liquid fuel is injected as a thin film on a solid pre-filmer

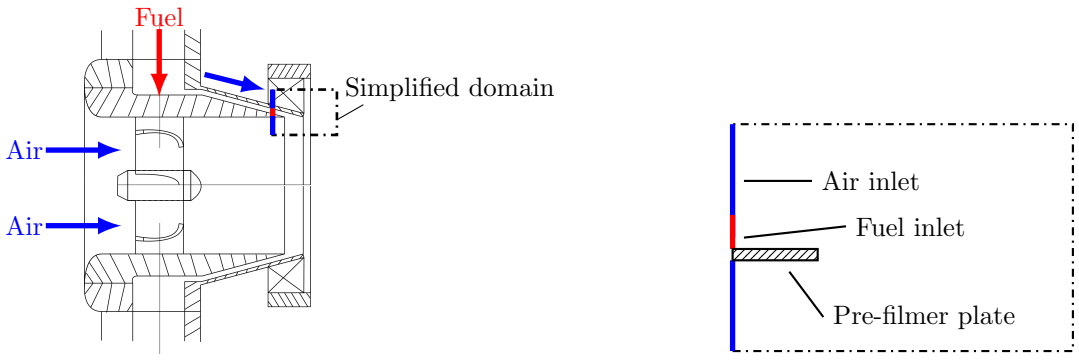

(a) Schematic view (b) Simplified domain

Figure 2: Schematic view of the planar pre-filming Airblast atomizer and simplified computational domain for numerical simulations.

plate which is then destabilized by the high speed air flowing above the liquid inlet and below the pre-filmer plate. It is to be remarked that the length of the computational domain along the downstream direction in this work is longer than that of the work of Warncke et al. [16]. The rationale behind having a longer downstream length of the computational domain are to accurately capture the characteristics and physics of

atomization of liquid droplets. The dimensions of the computational domain, pre-filmer plate and the height of the liquid fuel film used in the simulations along with the boundary conditions are marked in Figure 3 whose values are given in Table 1.

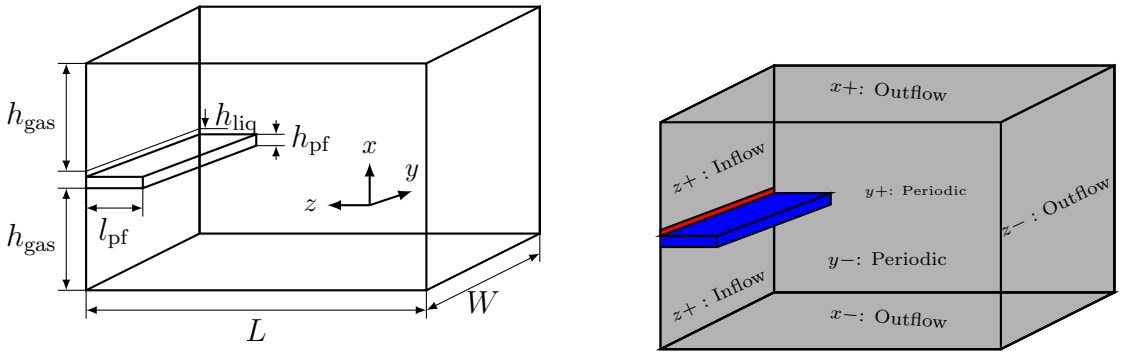

(a) Dimension of simulation domain

(b) Boundary conditions

Figure 3: Dimensions and boundary conditions used in the computational domain with red region representing fuel inlet and blue region depicting solid pre-filmer plate.

Table 1: Dimensions of computational domain.

L	W	h_{gas}	h_{liq}	l_{pf}	h_{pf}
6.6 mm	3.3 mm	1.5 mm	100 µm	1 mm	200 mm

The fuel and the air are injected along the $z+$ plane under an inflow boundary condition along with periodic boundary conditions imposed along the y direction (to mimic the annular combustor domain), and outflow boundary conditions on the remaining planes of the computational domain is imposed. The details of the boundary condition for each face of the computational domain is given in Table 2. However, the

Table 2: Summary of boundary condition for each face of the computational domain.

Coordinate direction	**Face**	**Boundary condition**
$x+$	Top face	Outflow
$x-$	Bottom face	Outflow
$y+$	Rear face	Periodic
$y-$	Front face	Periodic
$z+$	Left face	Inflow
$z-$	Right face	Outflow

chosen length of the pre-filmer plate l_{pf} measured 1 mm is smaller than the experimental setup [14]. It was found [14] that changes to this length have no significant impact on the atomization process and therefore is sufficient to reproduce the liquid film breakup. A boundary layer of gas on the liquid with thickness $\theta = 25.7\,\mu m$ is employed to take into effect the instability wave formation on the liquid phase due to high shear from the gas phase.

2.3. Operating conditions

The operating conditions employed in this work for the detailed numerical simulations are summarized in Table 3 where ρ is the density, ν is the kinematic viscosity, μ is the dynamic viscosity, r_ρ is the density ratio, r_ν is the kinematic viscosity ratio, q is the momentum flux ratio, Re is the Reynolds number, We is the Weber number, and $h_{chw} = 4\,mm$ is the half channel width of the injection channel in the annular combustor. The expressions for the non-dimensional numbers listed in this table are defined in Table 4.

Table 3: Summary of Operating Conditions.

Parameter	**SI Unit**	**Value**
Liquid Properties		
w_{liq}	m/s	0.5
ρ_{liq}	kg/m^3	770
ν_{liq}	m^2/s	2.03×10^{-6}
σ	kg/s^2	2.75×10^{-2}
Gas properties		
w_{gas}	m/s	50
ρ_{gas}	kg/m^3	1.2
ν_{gas}	m^2/s	1.5×10^{-5}
Non-dimensional numbers		
Re_{gas}	[-]	13,333
Re_{liq}	[-]	24.63
We	[-]	21.38
q	[-]	15.58
r_ρ	[-]	641.67
r_ν	[-]	13.6

Table 4: Expressions for non-dimensional numbers characterizing the flow.

$\text{Re}_{\text{liq}} = w_{\text{liq}} h_{\text{liq}} / \nu_{\text{liq}}$	$\text{Re}_{\text{gas}} = w_{\text{gas}} h_{\text{chw}} / \nu_{\text{gas}}$	$\text{We} = \rho_{\text{gas}} (w_{\text{gas}} - w_{\text{liq}})^2 h_{\text{pf}} / \sigma$
$q = \rho_{\text{liq}} w_{\text{liq}}^2 / \rho_{\text{gas}} w_{\text{gas}}^2$	$r_\rho = \rho_{\text{liq}} / \rho_{\text{gas}}$	$r_\nu = \nu_{\text{liq}} / \nu_{\text{gas}}$

The Weber number is computed based on the gas phase density, liquid and gas slip velocity, and thickness of the pre-filmer plate h_{pf} due to the significance of the impact on the ligament breakup length observed by Gepperth et al. [14]. The liquid fuel Shellsol D70 is used in the simulations for two reasons: first, its similar physical properties (specifically, viscosity μ and surface tension σ) at ambient temperature as that of the Jet A-1 fuel and second, its low surface tension (thereby promoting droplet breakup) that will be useful for its use in the simulations of primary atomization. Moreover, the experimental study [14] has employed Shellsol D70, hence, it will be beneficial to compare the results from the simulation with the experiments for the same fuel properties. Hence, having a smaller computational domain coupled with low surface tension will be beneficial to observe large number of physical atomization events.

The Reynolds and Weber number in the flows inside aircraft engines are very high leading to a highly turbulent flow condition. Such high turbulence often produce very small liquid structures which require high mesh resolution to be captured by a fixed grid interface reconstruction methods. Hence, in order to be computationally efficient to simulate the primary atomization of Airblast liquid sheet, we have chosen a moderate operating point with comparatively less Reynolds and Weber number with respect to the real-time aircraft engines. This chosen operating point corresponds to aircraft altitude relight condition [40, 41].

3. Numerical setup

3.1. Incompressible Navier–Stokes equations

The incompressible multiphase flows can be described by the following set of conservative form of the Navier-Stokes equations

$$\boldsymbol{\nabla} \cdot \boldsymbol{u} = 0, \tag{1}$$

$$\frac{\partial \rho \boldsymbol{u}}{\partial t} + \boldsymbol{\nabla} \cdot (\rho \boldsymbol{u} \otimes \boldsymbol{u}) = -\boldsymbol{\nabla} P + \boldsymbol{\nabla} \cdot (2\mu \boldsymbol{D}) + \boldsymbol{B}, \tag{2}$$

where $\boldsymbol{u}$ is the velocity field, ρ is the density, μ is the dynamic viscosity, P is the pressure field, $\boldsymbol{D}$ is the strain rate tensor given as $\boldsymbol{D} = \frac{1}{2}(\boldsymbol{\nabla u} + (\boldsymbol{\nabla u})^T)$, and $\boldsymbol{B}$ is the sum of the body and surface tension forces. $\boldsymbol{B} = \boldsymbol{B}_{\mathrm{b}} + \boldsymbol{B}_{\mathrm{st}}$ where $\boldsymbol{B}_{\mathrm{b}}$ is the force due to gravity (neglected in this work) and $\boldsymbol{B}_{\mathrm{st}}$ is the force due to surface tension which is given as $\boldsymbol{B}_{\mathrm{st}} = \sigma\kappa\delta_I \boldsymbol{n}$. σ represent the surface tension, κ is the curvature of the interface computed using the level set function ϕ according to

$$\kappa(\phi) = -\boldsymbol{\nabla} \cdot \left(\frac{\boldsymbol{\nabla}\phi}{\|\boldsymbol{\nabla}\phi\|_2} \right), \tag{3}$$

and δ_I is the Dirac delta function centered on surface of the interface.

Within the context of two-phase flows, an interface Γ separates the liquid and the gas phase. The material properties such as density and viscosity are assumed to be constant within each phase, i.e., $\rho = \rho_{\mathrm{liq}}$ and $\mu = \mu_{\mathrm{liq}}$ in liquid phase and $\rho = \rho_{\mathrm{gas}}$ and $\mu = \mu_{\mathrm{gas}}$ in gaseous phase. However, these properties are subject to a jump at the location of the liquid/gas interface. This jump is written as $[\rho]_\Gamma = \rho_{\mathrm{liq}} - \rho_{\mathrm{gas}}$ and $[\mu]_\Gamma = \mu_{\mathrm{liq}} - \mu_{\mathrm{gas}}$ while the velocity field remains continuous across the interface, hence $[\boldsymbol{u}]_\Gamma = 0$. However, the pressure is not continuous across the interface and it is possible to write the pressure jump [42] across the interface as

$$[P]_\Gamma = \sigma\kappa(\phi) + 2[\mu]_\Gamma (\nabla \boldsymbol{u} \cdot \boldsymbol{n}) \cdot \boldsymbol{n}, \tag{4}$$

where $\boldsymbol{n}$ is the unit normal of the liquid/gas interface pointing towards the liquid phase in a computational cell.

3.2. Flow solver

To simulate the primary atomization of Airblasted liquid sheet, we use in-house Navier-Stokes equation solver ARCHER [43] in this work. The capabilities of ARCHER have been presented many of the previous works [44, 45, 46, 47]. This solver is structured, parallel, and developed for direct numerical simulations (DNS) of complex and turbulent multiphase flows with the application to study primary atomization of liquid jet. The liquid/gas interface is represented by level set contiguous signed distance function and the mass conservation in the computational domain is ensured using volume fraction (see Section 3.3 for more details). This solver has been validated for various cases of complex turbulent flow configurations [48, 49, 50] thus, the numerical methods employed in this solver are tailored for treating turbulence in the system.

A staggered grid configuration is used with central finite difference scheme for least numerical dissipation. The scalar variables such as liquid volume fraction, density, viscosity, level set function, and pressure are stored in the cell center while the vector variables such as components of velocity and vorticity are stored in cell faces. A consistent mass and momentum flux computation [44] technique is employed in the solver that facilitates to perform simulations of large density ratio between liquid and gas phases.

A second-order central difference scheme is employed for discretization of the spatial derivatives to avoid any dissipation. However, the convection term is discretized using fifth-order WENO scheme to ensure a robust behavior of the solution. A semi-implicit formulation proposed by Sussman et al. [51] is used for discretizing the viscous term yielding second-order accuracy in regions away from the liquid/gas interface and first-order accuracy near the interface. A ghost fluid method (GFM) [52] is employed for the spatial discretization of the Poisson equation for taking into account the force due to surface tension as a pressure jump. The resulting linear system of symmetric and positive definite matrix with five diagonals is solved

using multigrid algorithm for preconditioning a conjugate gradient (CG) method [53]. A projection method with a predictor-corrector time integration scheme is used to solve the Navier-Stokes equation with the time step size Δt determined based on the Courant-Friedrichs-Lewy (CFL) condition. The reader is referred to Ref. [44, 43] for more details on the implementation of the numerical methods, schemes, and solution algorithm employed in the ARCHER solver.

The shape and walls of the solid pre-filmer plate are reproduced using staircase immersed boundary method (SIBM) similar to that described by Vu [54]. The SIBM is a form of the immersed boundary method (IBM) approximates the shape of the boundary such that it falls onto the Cartesian grid lines. The walls of the pre-filmer plate are treated as non-wetting walls used in the boundary condition of the liquid film injected on the plate. It is to be remarked that no solid-liquid wetting model is used for the liquid film injection on the plate in ARCHER solver. The representation of the walls of this pre-filmer plate by the SIBM technique is depicted in Figure 4.

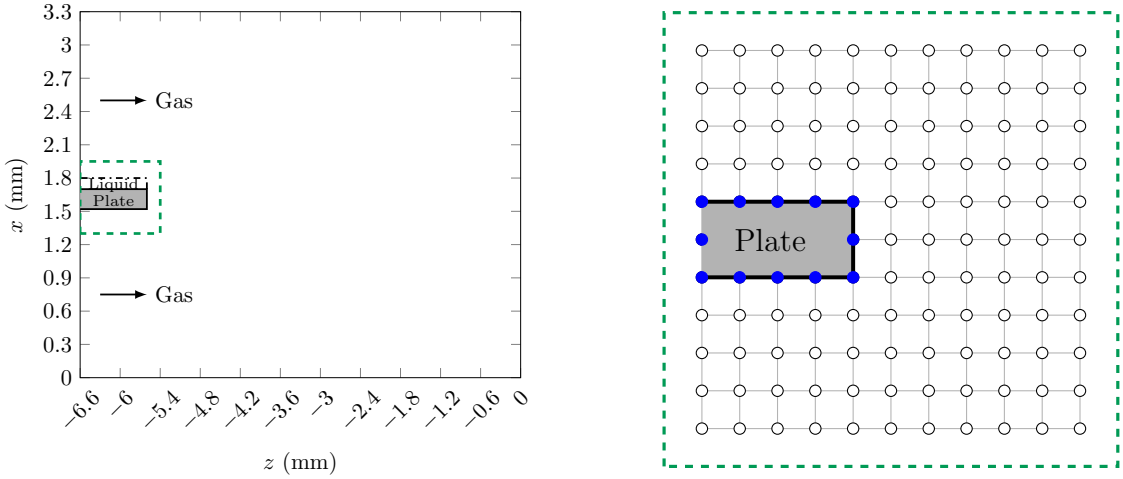

Figure 4: Illustration of solid pre-filmer plate representation (left figure) using staircase immersed boundary method (SIBM) with a zoomed view in (right figure). The blue filled circles in the right figure represent the grid points on the surface of pre-filmer plate and white unfilled circles represent the grid points in the rest of the computational domain.

A turbulent velocity profile is imposed at the inlet $z+$ plane (c.f. Figure 3b) for the liquid and gas phases. The turbulence in the simulations is initiated in the gas phase using synthetic turbulence method [55]. The turbulent fluctuations in the velocity of the gas phase w'_{gas} is set to 10% of the bulk gas velocity w_{gas} at the plane of gas injection, i.e., $w'_{\text{gas}} = 0.1 w_{\text{gas}}$. The turbulent integral length scale is set to 3% of the total gas channel height h_{gas}, i.e., $l_t = 0.03 \times (2h_{\text{gas}})$ (refer Table 1). With the injected velocity flucutations and the chosen turbulent length scale, the turbulent Reynolds number is determined to be $Re_\tau = u' l_t / \nu_{\text{gas}} \approx 80$. Based on the relation $\eta / l_t \sim (Re_\tau)^{-3/4}$ [56] for single phase constant density and constant viscosity flows, we get the Kolmogorov length scale in the gas phase to be $\eta \approx 3.36\,\mu\text{m}$. Hence, according to Equation 9.6 in Pope [56], the relation between the required minimum mesh spacing and the Kolmogorov length scale is given as

$$\frac{\Delta x_{\min}}{\eta} \approx 2, \tag{5}$$

i.e., a mesh spacing about twice the size of the smallest eddy (Kolmogorov length scale) is required to fully resolve all scales of turbulent motion in a single phase flow. However, this work deals with two-phase flows in which the liquid/gas interface is assumed to be of infinitesimal thickness. This means that the scales of motion are considered well resolved at the limit of the infinitesimal interfacial thickness which is challenging to achieve for two-phase flows simulations [57] with our available computational resources [58]. Nevertheless, this relation could be considered to give an estimated value of the required minimum mesh spacing based on the Kolmogorov length scale.

3.3. Numerical method

Within the context of two-phase flows, it is imperative to track the location of the liquid/gas interface to accurately capture the flow physics. In order to accurately capture and track this interface, we use a hybrid moment of fluid–level set (HyMOFLS) method [59]. The HyMOFLS interface reconstruction method uses moment of fluid (MOF) method [43] and the level set (LS) framework from the coupled level set volume of fluid (CLSVOF) method [42]. A piecewise linear interface calculation (PLIC) technique is employed in this method in which the interface is reconstructed as three dimensional planes. The methodology involved in the HyMOFLS method is described in the following subsections.

3.3.1. Moment of fluid (MOF) method

As mentioned above, the HyMOFLS is an amalgamation of the MOF and LS (from the CLSVOF method) frameworks of interface reconstruction. In this subsection, we present the methodology and the algorithm involved in the MOF method of interface reconstruction. The moment of fluid (MOF) method [60, 61, 43] can be considered as a generalized VOF method. This because this method uses liquid volume fraction F as well as centroids $\boldsymbol{x}_{\mathrm{COM}}$ of liquid and gas phases in each computational cell to reconstruct the liquid/gas interface. With the 3D planar representation of the interface from PLIC technique, the equation of the interface is $ax + by + cz + d = 0$ with the unit normal of this interface determined to be $\boldsymbol{n} = [a, b, c]^T$. The position and orientation of the interface are governed by the parameters d and $\boldsymbol{n}$ respectively. The MOF method of interface reconstruction computes the accurate values of the parameters d (defining the position of the interface) and $\boldsymbol{n}$ (defining the orientation of the interface) through the solution to the following equations:

$$\left|F^{\mathrm{ref}} - F^{\mathrm{act}}(\boldsymbol{n}, d)\right| = 0, \text{ and} \tag{6}$$

$$E^{\mathrm{MOF}}(\boldsymbol{n}, d) = \left\|\boldsymbol{x}^{\mathrm{ref}}_{\mathrm{COM}} - \boldsymbol{x}^{\mathrm{act}}_{\mathrm{COM}}(\boldsymbol{n}, d)\right\|_2 . \tag{7}$$

On one hand, the interface position d is determined by conserving the liquid (and gas) phase volume between the reference (original) and actual (reconstructed) interfaces as demonstrated by the solution of Equation (6) where F is the liquid volume fraction in a computational cell. The liquid volume fraction F is defined as the ratio of the volume of liquid to that of the computational cell and hence $F \in [0, 1]$. The gas phase volume fraction can be determined in a straightforward manner as $F^{\mathrm{gas}} = 1 - F$. The phase based properties such as density ρ and viscosity μ are obtained according to $\alpha = \alpha_{\mathrm{liq}} F + \alpha_{\mathrm{gas}}(1 - F)$ where $\alpha = [\rho, \mu]$. On the other hand, the accurate orientation of the interface $\boldsymbol{n}$ is determined by solving the Equation (7) in which the E^{MOF} represent the centroid defect. It is defined as the Eucledian distance between the reference and actual centroids of the reference and actual interfaces respectively. The idea of the MOF method is depicted in the Figure 5 for a two dimensional computational cell configuration with liquid phase centroids.

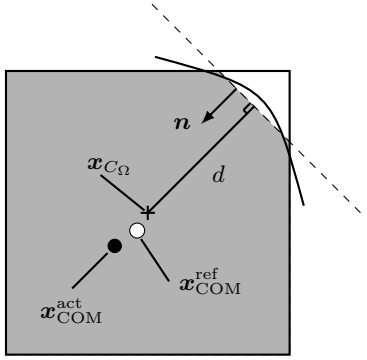

Figure 5: Exemplary computational cell in two dimensions with reference (original) and actual (reconstructed) liquid phase centroids.

The methodology of solving the Equations (6) and (7) involves first choosing a reference phase whose centroid is farthest from the computational cell centre. The rationale behind choosing the reference phase in this manner lies behind the fact that the phase with farthest centroid (i.e., phase with the least volume) has highest sensitivity towards the orientation of the liquid/gas interface. Next, the value of d is obtained by conserving volume upto machine precision to the solution of Equation (6) by a geometric method [62]. Once the value of d is obtained, an initial guess to the unit normal $\boldsymbol{n}$ is determined from the level set function in the ARCHER solver. Then, the centroid defect E^{MOF} is minimized through Gauss-Newton iterative algorithm. For detailed explanation, algorithms, and code implementations of the MOF method, the reader is referred to [43].

The advection of the interface within the framework of MOF method involves advection of liquid volume fraction as well as the liquid and gas phase centroids. The transport of liquid volume fraction is governed by

$$\frac{\partial F}{\partial t} + \boldsymbol{u} \cdot \boldsymbol{\nabla} F = 0, \tag{8}$$

solved using a directionally split advection algorithm [63]. The transport of the liquid and gas phase centroids is performed according to

$$\frac{\partial \boldsymbol{x}_{\mathrm{COM}}}{\partial t} = \boldsymbol{u}(\boldsymbol{x}_{\mathrm{COM}}), \tag{9}$$

where $\boldsymbol{u}(\boldsymbol{x}_{\mathrm{COM}})$ is the velocity at the location of the centroid $\boldsymbol{x}^{\mathrm{ref}}_{\mathrm{COM}}$ linearly interpolated from the cell face-centered velocity. The reader is referred to Appendix A of Ref. [60] for the detailed derivation of the Equation (9). This transport equation is solved using a directionally-split advection algorithm with an Eulerian Implicit–Lagrangian Explicit (EI–LE) scheme, more details can be found in Ref. [43].

3.3.2. Coupled level set volume of fluid (CLSVOF) method

The CLSVOF method employed in this work, within the context of HyMOFLS framework, follows the study of Ménard et al. [42]. In this study, the level set signed distance function ϕ defines the location of the interface the VOF method is used in conjunction to for the purpose of conservation of mass. Within the context of CLSVOF method, the parameters of the liquid/gas interface, i.e., d is determined by geometric method [62] and $\boldsymbol{n}$ is determined according to the methodology described by Ménard et al. [42]. The equation, methodology, and numerical method involved in transport of the level set function is performed the same was as for the liquid volume fraction (see Equation (8)). The coupling between the level and VOF method within the context of CLSVOF method involves the mutual correction of the values performed simultaneously conserving the liquid volume and the computation of the interface curvature is not affected. The implementation of the level set advection, correction and coupling with VOF method is performed similar to a classical CLSVOF method [64]; details of it are not recalled here.

3.3.3. Hybrid moment of fluid–level set (HyMOFLS) method

The MOF method is relatively more accurate than the CLSVOF method [43], however requiring higher computational cost [65]. In fact, it has been shown [43] that MOF method is accurate in capturing the interface in the under-resolved regions of the flow than the CLSVOF method. Therefore, the rationale behind the development of HyMOFLS framework [59] is to use MOF method for the interface reconstruction in the simulations only when it is necessary, i.e., in the under-resolved regions of the flow. Such regions are identified through the proposition [59] of the parameter called interface resolution quality (IRQ) defined as

$$\mathrm{IRQ} = \frac{1}{\kappa \Delta x}, \tag{10}$$

where κ and Δx correspond to the local interface curvature and local mesh spacing respectively. The following criterion is checked in each computational call to choose between MOF and CLSVOF methods of interface reconstruction in it.

$$\mathrm{IRQ} = \frac{1}{\kappa \Delta x} = \begin{cases} < 2, \Rightarrow \text{Under-resolved structure} \Rightarrow \text{Use MOF method}, \\ \geq 2, \Rightarrow \text{Resolved liquid structure} \Rightarrow \text{Use CLSVOF method}. \end{cases} \tag{11}$$

In order to reduce the computational expense even further in the HyMOFLS method, this criterion is checked in the cells in the neighborhood of the interface as shown in Figure 6 where the solid line represent the liquid/gas interface, red cells correspond to the MOF method tagging while the blue cells to the CLSVOF method tagging. Each MOF tagged cell has a flag with a value 1 while each CLSVOF tagged cell has a flag value of 0. As can be seen from this figure, the MOF method is tagged only in the cells with high curvature change (often a characteristic of under-resolved interfacial structures) while the CLSVOF method is tagged for the remainder regions.

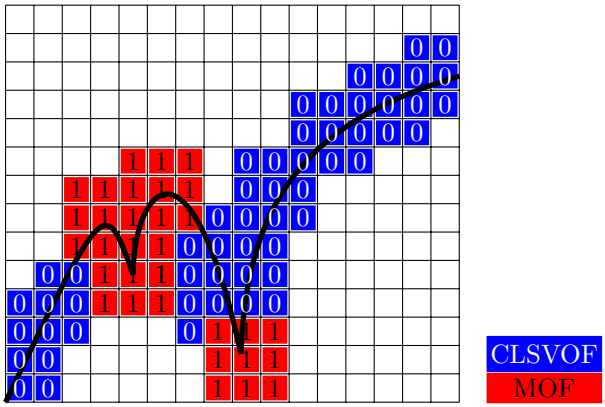

Figure 6: Narrow band of the MOF method tagged cells (red cells with value 1) and CLSVOF method tagged cells (blue cells with value 0) around the liquid/gas interface (shown in black solid line).

3.4. Simulation cases investigated

This paper aims to investigate the primary atomization of Airblasted liquid sheet and extract the atomization characteristics. The specific focus of this work lies on the effect of inlet velocity profile (for the liquid and gas phases) on the atomization characteristics. To that end, we perform two sets of simulations imposing two different velocity profiles on the liquid and gas inlet – first, flat profile (Fp) (also called plug flow profile) for liquid phase and gas phase (shown in Figure 7a) and second, a turbulent channel flow velocity profile (Cp) for gas phase and a linear velocity profile for liquid phase (ranging from 0 to $2u_{\text{liq}}$) (shown in Figure 7b). The plots of these velocity profiles for each simulation case is shown in Figure 7. The equations for the velocity for the flat profile (Fp) case are given as

$$
\begin{aligned}
u &= 0 \\
v &= 0 \\
w &= \begin{cases} -w_{\text{gas}}, & 0 \le x < h_{\text{gas}} \\ 0, & h_{\text{gas}} \le x < h_{\text{gas}} + h_{\text{pf}} \\ -w_{\text{liq}}, & h_{\text{gas}} + h_{\text{pf}} \le x < h_{\text{gas}} + h_{\text{pf}} + h_{\text{liq}} \\ -w_{\text{gas}}, & h_{\text{gas}} + h_{\text{pf}} + h_{\text{liq}} \le x \le 2h_{\text{gas}} + h_{\text{pf}} + h_{\text{liq}}, \end{cases}
\end{aligned} \tag{12}
$$

and the equations for the velocity for the channel profile (Cp) case are given as

$$
\begin{aligned}
u &= 0 \\
v &= 0 \\
w &= \begin{cases} w_{\text{gas},1} & 0 \le x < h_{\text{gas}} \\ 0, & h_{\text{gas}} \le x < h_{\text{gas}} + h_{\text{pf}} \\ -\left(\frac{2w_{\text{liq}}}{h_{\text{liq}}+\Delta x/2}\right)(x - (h_{\text{gas}} + h_{\text{pf}})) & h_{\text{gas}} + h_{\text{pf}} \le x < h_{\text{gas}} + h_{\text{pf}} + h_{\text{liq}} \\ w_{\text{gas},2} & h_{\text{gas}} + h_{\text{pf}} + h_{\text{liq}} \le x \le 2h_{\text{gas}} + h_{\text{pf}} + h_{\text{liq}} \end{cases}
\end{aligned} \tag{13}
$$

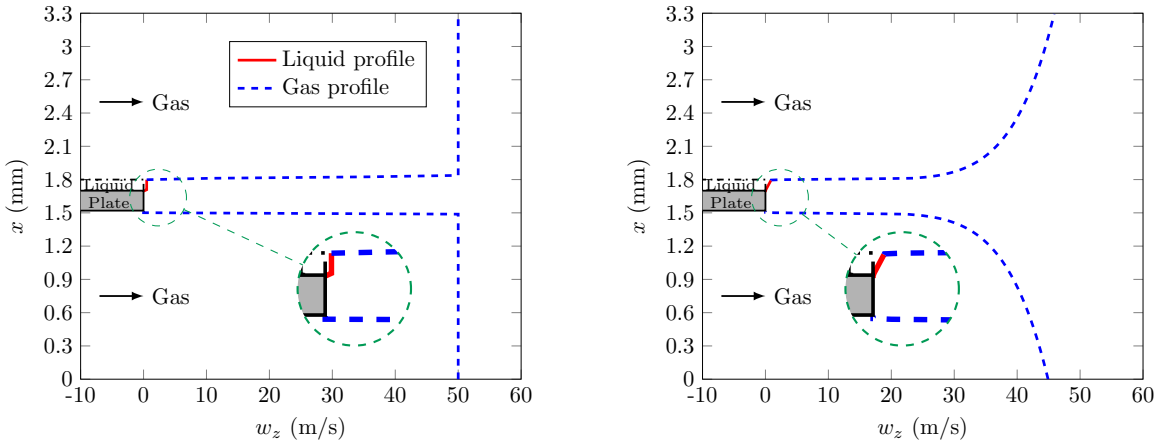

(a) Flat profile (Fp)

(b) Channel flow profile (Cp)

Figure 7: Velocity profile plots for liquid phase (——) and gas phases (- - -). In (a): flat profile (plug flow) for liquid and gas phases; (b) linear velocity profile for liquid and channel flow profile for gas phase.

where the values of $w_{\text{gas},1} = -w_{\max}\left(1 - \frac{|x-(h_{\text{liq}}-h_{\text{chw}})|}{h_{\text{chw}}}\right)^{1/7}$ and $w_{\text{gas},2} = -2w_{\text{liq}} - w_{\max}\left(1 - \frac{|x-(h_{\text{gas}}+h_{\text{pf}}+h_{\text{liq}}+h_{\text{chw}})|}{h_{\text{chw}}}\right)^{1/7}$ with $w_{\max} = \left(2^{20/7}/7\right) w_{\text{gas}}$ and the values of other domain-related variables can be referred to Table 1. For each simulation case, the computational domain (Figure 3a) is discretized using a mesh resolution of equidistant mesh spacing $\Delta x = 12.89\,\mu\text{m}$. The cases analyzed in this study are given in Table 5.

Table 5: Cases analyzed using numerical simulations with Fp representing flat profile for gas and liquid phases and Cp representing channel flow profile for gas phase and linear profile for liquid phase.

Mesh spacing (Δx)	**Velocity profile**	
	Flat profile (Fp)	Channel profile (Cp)
12.89 µm	c_1^{Fp}	c_2^{Cp}

4. Results and discussion

We now present the results from the simulation of the primary atomization of the Airblasted liquid sheet. First, qualitative analyses of the breakup physics and atomization mechanisms will be presented. A comparison of these mechanisms will be made between the two inlet velocity profile simulation cases. Then, quantitative data extracted from the simulations, such as drop size distribution (DSD) and drop velocity distribution (DVD), are presented. These quantities are vital for the subsequent Lagrangian particle simulations for the secondary atomization of drops. To investigate the presence of secondary atomization of the drops occurring in the simulations, the DSD and number based frequency distribution of drop diameters along with the drop-based Weber number at different downstream sampling locations are compared. Following the secondary atomization studies, the extraction of near-field quantities such as lengths and velocities of liquid ligaments formed in the accumulated liquid region at the edge of the pre-filmer plate. It is to be remarked that this work is one among the initial studies [35, 16] in which such a novel methodology of extraction such near-field data is employed.

4.1. Breakup mechanisms

The Airblast atomization process is comprised of many breakup mechanisms of which two predominant mechanisms found in the literature [35, 14] are sheet/bag breakup and ligament breakup. These droplet breakup mechanisms are observed in our simulations for both the inlet velocity profile cases. Figures 8 and 9 show several instantaneous snapshots of the liquid/gas interface shown in blue color (obtained as the zero isolevel of the level set function) for the flat profile (Fp) and channel profile (Cp) simulation cases respectively. The flow of the liquid and gas is from the top to bottom in these figures. The breakup process in the planar pre-filming Airblast atomization is as follows: due to difference in the momentum flux between liquid and gas phases, instability waves are generated in the liquid sheet on top of the pre-filmer plate (c.f. Figure 8b) causing liquid shear thereby collecting the liquid parcel towards the trailing edge of the pre-filmer plate (see Figure 1) forming a liquid reservoir. From this reservoir, thin sheets and long ligaments of liquid are formed (c.f. Figure 8b) which then develop holes (c.f. Figure 8d) since the surface tension cannot counteract the disintegration process. The holes penetrate the sheet causing breakup into various sized droplets (c.f. Figure 8d) and long ligaments break up into bulgy and medium-sized droplets (c.f. Figure 8e). These observations are consistent to the torn sheet/bag breakup regime described by Fernández et al. [66] for the operating point employed in this work. The first observation from these figures is that the waves formed on the liquid film/sheet over the pre-filmer plate are visible; these waves are caused by the shear due to the difference in the velocity and density of the liquid and gas phases. It is speculated that these waves are formed due to the Kelvin-Helmholtz (KH) instability, however, this conjecture is still to be verified. The next observation is that there exists a global qualitative similarity in the destabilization of the interface is observed between the simulation cases. It is to be remarked that there was no dewetting of the plate is observed in the simulations. Moreover, the flapping of the liquid sheet (observed in side view $x - z$ plane) was found to be asynchronuous to the atomization, i.e., the frequency at which droplets and ligaments detatch from the liquid sheet is different from the frequency of the flapping of the sheet. The quantification of these frequencies is beyond the scope of this work.

To get a global picture of the sheet flapping, atomization, and the turbulent velocity imposed, Figure 10 shows two instantaneous snapshots from flat profile (Fp) and channel profile (Cp) along with the contours of the velocity magnitude. From this figure, it is indeed obvious that the velocity field is highly turbulent causing the destabilization of the liquid sheet and its subsequent atomization. Moreover, we can observe the disintegration of large drops and formation of thin sheet as well as long ligaments at the trailing edge of pre-filmer plate.

4.1.1. Sheet/bag breakup

One of the dominant droplet breakup mechanisms observed in the Airblast atomization simulations is the sheet/bag breakup. Figure 11 shows a series of instantaneous snapshots of the visualization of the liquid sheet breakup into drops for the flat profile (Fp) inlet velocity profile simulation case c_1^{Fp}. In this breakup mechanism, the accumulated liquid at the trailing edge of the pre-filmer plate forms a bag like structure (c.f. Figure 11a) which is then pushed up due to the aerodynamic forces from the high speed air flowing below the pre-filmer plate. This bag then develops holes (c.f. Figure 11b) partly due to the surface tension failing to counteract the disintegration phenomenon (i.e., physical effect) and partly due to the mesh resolution employed in the simulations (i.e., numerical effect). This hole quickly penetrates through the surface of the sheet (c.f. Figure 11c) thereby forming droplets (c.f. Figure 11d) whose diameters are of the size of the thickness of the sheet. Such a sheet/bag breakup mechanism is commonly found in the flows with high shear. It is to be remarked that an identical physical mechanism of sheet breakup is observed in the channel profile (Cp) simulation case c_2^{Cp}.

4.1.2. Ligament breakup

The next predominant breakup mechanism observed in the simulations is the ligament breakup mechanism. Figure 12 shows a series of instantaneous snapshots of the flow visualization extracted from the simulation case of flat profile (Fp) c_1^{Fp}. The liquid accumulated as reservoir at the trailing edge of the pre-filmer plate (see Figure 1 for the location of trailing edge) forms ligaments. These ligaments, shown in

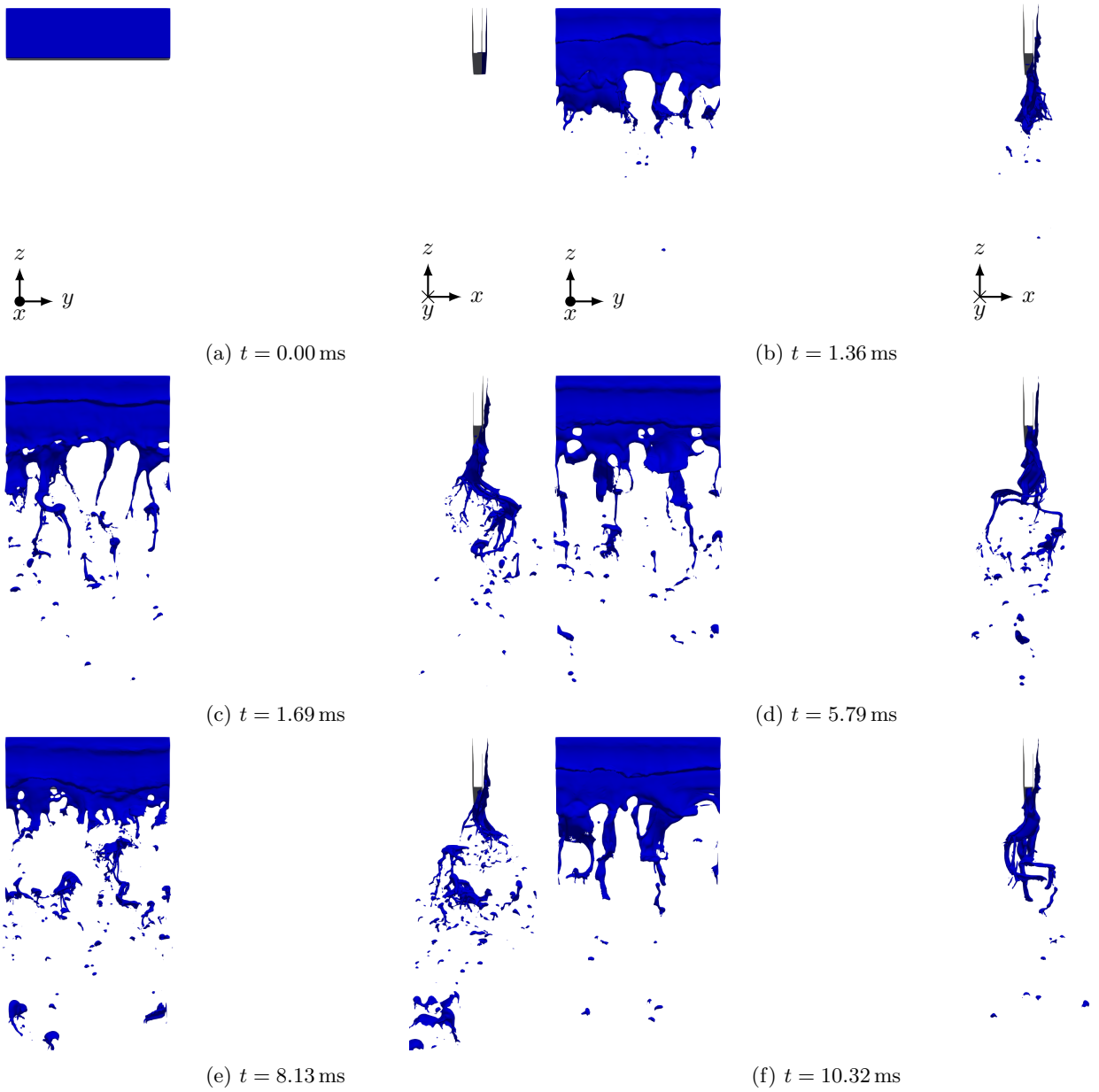

(a) $t = 0.00\,\mathrm{ms}$ (b) $t = 1.36\,\mathrm{ms}$

(c) $t = 1.69\,\mathrm{ms}$ (d) $t = 5.79\,\mathrm{ms}$

(e) $t = 8.13\,\mathrm{ms}$ (f) $t = 10.32\,\mathrm{ms}$

Figure 8: Instantaneous snapshots of liquid sheet destabilization and atomization into ligaments and droplets for the flat profile (Fp) simulation case c_1^{Fp}.

Figure 12a, are subjected to high aerodynamic forces from the air flowing above and below the pre-filmer plate. These forces stretch the ligament (c.f. Figure 12b) upto a point when its diameter is smaller than the employed computational mesh spacing. It is at this point the breakup of the ligaments into droplets (of the size of diameter of ligaments) occur due to Rayleigh-Plateau instability (c.f. Figures 12c and 12d).

For the purposes of illustration, Figure 13 show instantaneous snapshots of the different breakup mechanisms along with the cluster of produced droplets rendered using Blender visualization software for the case $c_{11,\mathrm{Fp}}^{\mathrm{CLSVOF}}$.

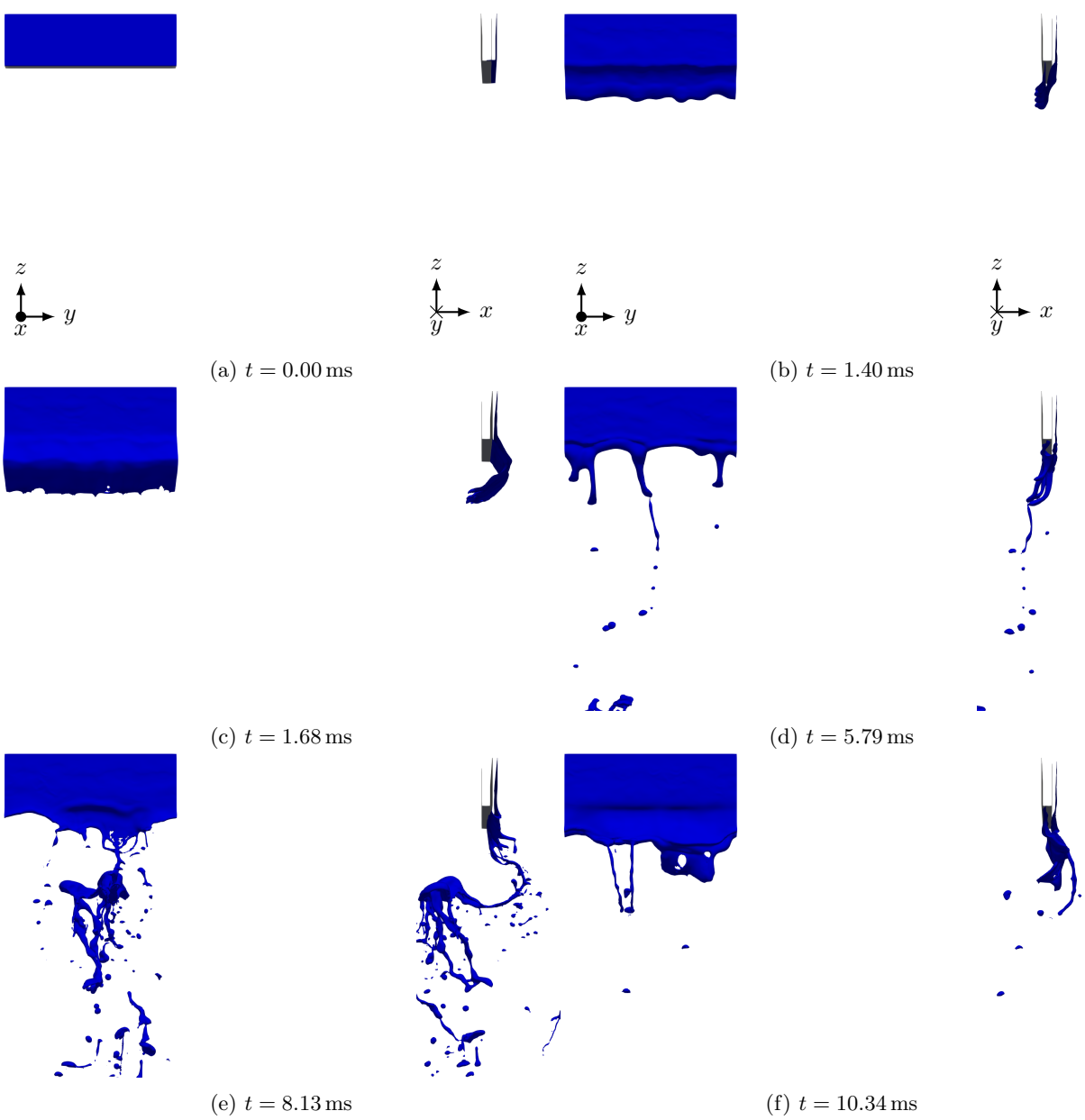

(a) $t = 0.00\,\mathrm{ms}$ (b) $t = 1.40\,\mathrm{ms}$

(c) $t = 1.68\,\mathrm{ms}$ (d) $t = 5.79\,\mathrm{ms}$

(e) $t = 8.13\,\mathrm{ms}$ (f) $t = 10.34\,\mathrm{ms}$

Figure 9: Instantaneous snapshots of liquid sheet destabilization and atomization into ligaments and droplets for the channel profile (Cp) simulation case c_2^{Cp}.

4.2. Droplet analysis

Having presented the qualitative results so far, we now present the quantitative results pertaining to the atomized drops in this subsection. Among the many quantitative results extracted from the simulations, the drop size distribution (DSD) and drop velocity distribution (DVD) are pivotal in designing the combustion chamber of the aero engines. The size of the droplet has a direct influence on its rate of fuel evaporation and its subsequent combustion. In fact, the DSD and DVD are also useful for secondary atomization simulations using Lagrangian and Eulerian approaches and primary atomization modeling for which the droplets of certain size are injected along a specific trajectory with a certain velocity [67]. Therefore, it is imperative to understand and analyze the DSD and DVD for the retro-improvement of the injector design. In order to

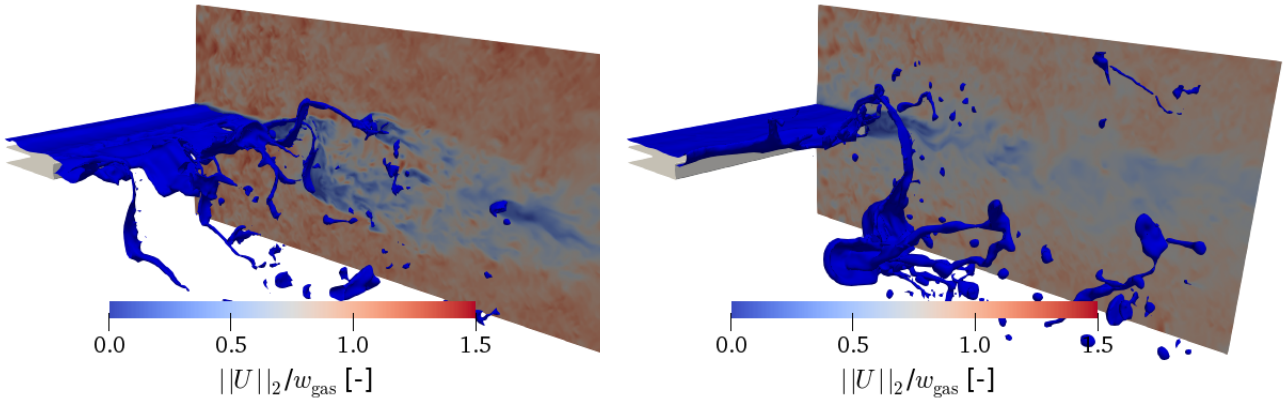

(a) Flat profile (Fp) (b) Channel profile (Cp)

Figure 10: Instantaneous snapshots of the atomizing liquid sheet along with the contour of the velocity magnitude for flat profile (Fp) and channel profile (Cp) case.

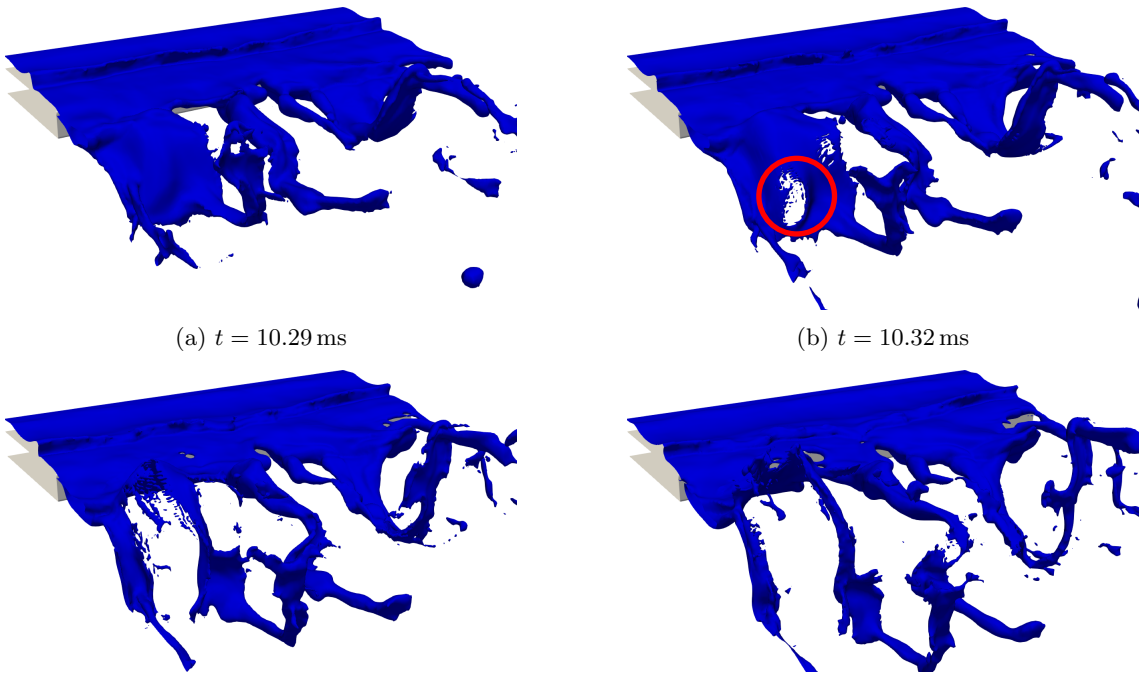

(a) $t = 10.29\,\text{ms}$ (b) $t = 10.32\,\text{ms}$

(c) $t = 10.36\,\text{ms}$ (d) $t = 10.39\,\text{ms}$

Figure 11: Sequence of events of sheet/bag breakup mechanism in Airblast atomization visualized from simulations using flat profile (Fp) inlet velocity case. (a): formation of liquid bag and sheet-like structure; (b): hole formation and liquid sheet rupture; (c) and (d): sheet breakup into droplets.

obtain these distributions, the extraction of atomized droplet (or a liquid structure) from the simulations is necessary. To that end, such liquid structures are identified using a connected component labelling (CCL) structure detection algorithm [68] for each sampled time step. Each sampling from the simulations is written to disk approximately every 35 µs of physical time containing the three dimensional data of the computational domain including velocity, level set, liquid volume fraction data along with the statistical information about the liquid structures. The information collected for each liquid structure include their total volume, total

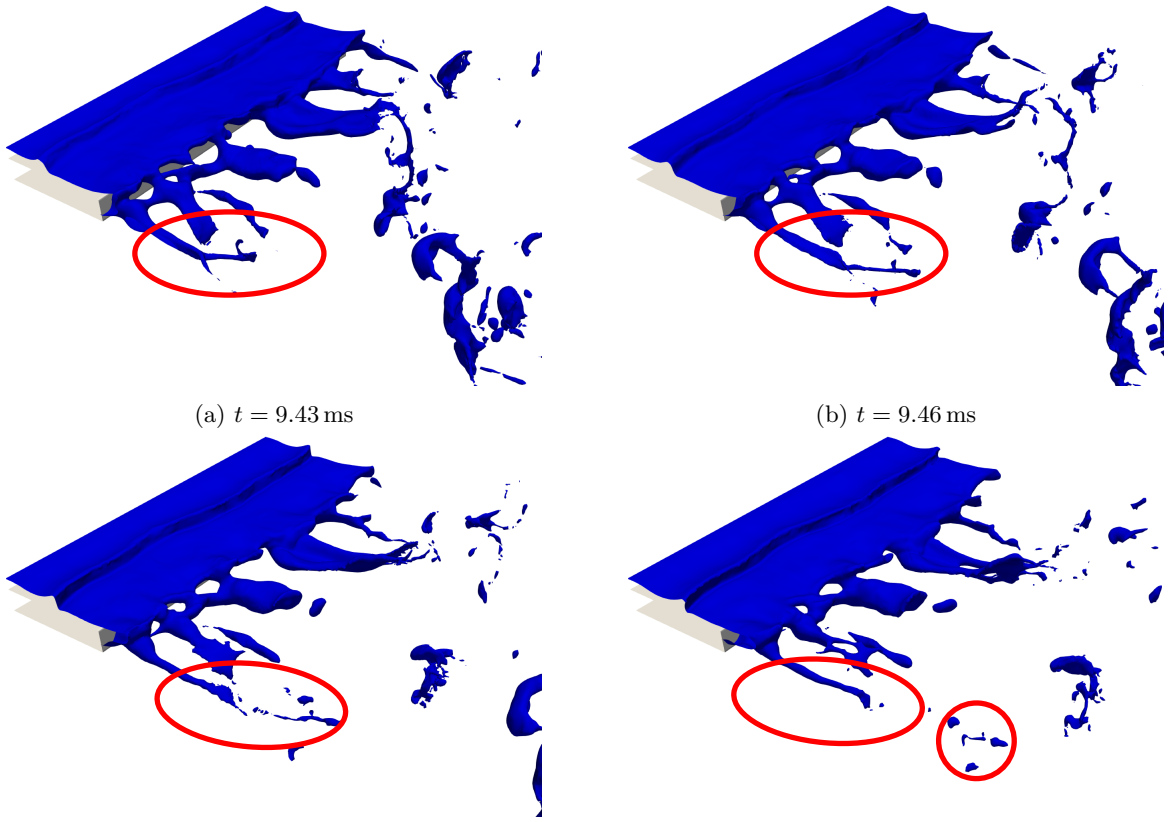

(a) $t = 9.43\,\text{ms}$ (b) $t = 9.46\,\text{ms}$

(c) $t = 9.50\,\text{ms}$ (d) $t = 9.53\,\text{ms}$

Figure 12: Sequence of events for ligament breakup of Airblast atomization visualized from simulations for flat profile (Fp) inlet velocity case. (a): formation of ligament from accumulated liquid; (b): stretching and twisting of ligament due to high speed of air; (c): ligament breakup due to Rayleigh-Plateau instability; (d): atomized droplets advected by high speed air.

surface area (computed as the sum of the area of PLIC interface spanning over all computational cells belonging to this structure), velocity (volume-weighted velocity from each cell weighted by total volume), and coordinates of the centroid of the structure. The total volume of each of these liquid structures (i.e., drops) is then computed using which an equivalent spherical diameter of each droplet is computed.

4.2.1. Drop size distribution

The drop size distribution (DSD) gives the information about the range of the droplet diameters and their probability of presence realized from injection. To construct this distribution from the simulation data, the droplets deteced using the CCL algorithm and their attributes are collected at the downstream exit plane of the computational domain. The collected drop diameters (d_{drop}) are binned to obtain a probability density function (PDF) of the drop size distribution (DSD).

Figure 14 shows the plot of the PDF of DSD for the Fp and Cp simulation cases along with the experimental data [16]. It can be seen that the profile of the experimental data [16] is multi-modal distribution indicating the presence multiple breakup mechanisms for the atomization in this configuration. However, there are two dominant peaks in this profile which could be attributed to the sheet and ligament breakup. It is hypothesized in this work that the first peak belongs to the remnants of sheet breakup (droplets and web of ligaments) while the second peak to the remnants of ligament breakup albeit this conjecture need to be validated. It is noteworthy to mention that the drops produced from the sheet breakup would be of the same size of the sheet thickness, hence, is very challenging to capture using the considered mesh resolutions in this work. However, the web of ligaments produced from the sheet breakup mechanism are large enough to be

(a) Rendering of the sheet breakup from the simulations.

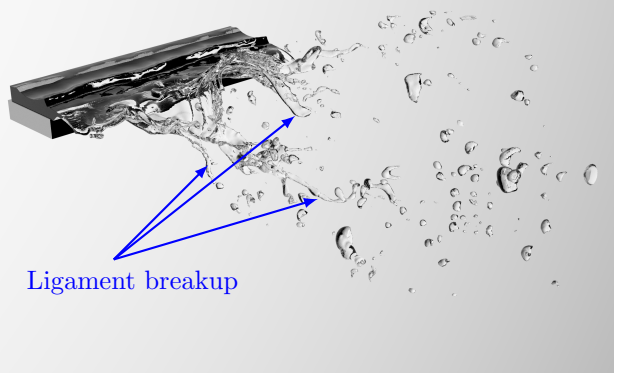

(b) Rendering of the ligament breakup from the simulations.

(c) Rendering of varying sized droplets produced.

Figure 13: Predominant breakup mechanisms observed in Airblast atomization simulations for the flat profile (Fp) c_1^{Fp} case.

captured and are hypothesized to be the cause of the first peak in the PDF of the DSD. This is because the thickness of the sheet are many orders of magnitude smaller in comparison to the diameter of the ligaments, hence, the sheet breakup is anticipated to produce smaller sized droplets than those from ligament breakup. However, it is to be noted that this hypothesis still need to be verified to confirm distinction between the dominant peaks in the profile of the DSD. It is to be remarked that the smallest diameter measured in the experiments is 20 µm, hence, the cut-off of the PDF of the DSD in the experimental profile. A previous work on the Airblasted liquid sheet [16] removed (i.e., clipped) the drops whose sizes are smaller than 20 µm when constructing the PDF of DSD for the sake of comparison with the experimental data. However, such a procedure will alter the profile of the PDF of the DSD giving a skewed measure of the DSD. To represent the

complete PDF, no such clipping or removal of the drops whose diameter is smaller than 20 µm is performed in this work.

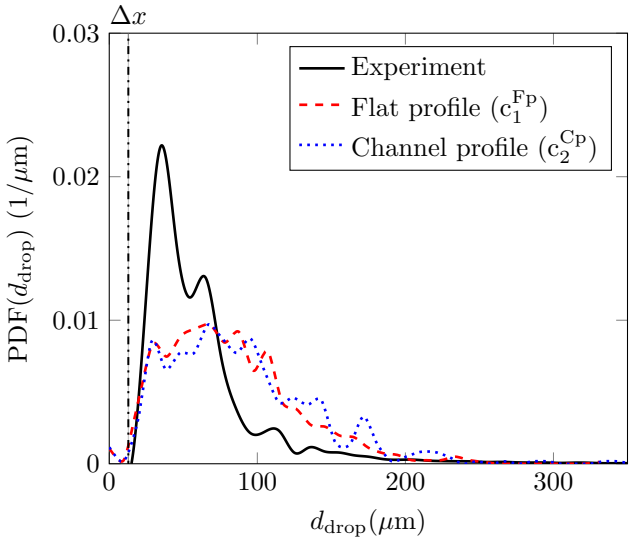

Figure 14: Plot of drop size distribution (DSD) for flat profile (Fp) c_1^{Fp} (- - -) and channel profile (Cp) c_1^{Cp} (·····) inlet profile cases from the simulations along with experimental data (——) [16]. The dashdotted line (-·-·-) represents the level of the mesh spacing $\Delta x = 12.89\,\mu\text{m}$ in comparison to the drop diameter d_{drop}.

The first inference from Figure 14 is that the simulation results are under-predicting the experimental data which could be attributed to the employed mesh resolution in the simulations. In fact, a similar under-prediction was also found in the study by Warncke et al. [16] using a diffused interface VOF method of liquid/gas interface reconstruction. Having a finer mesh resolution will indeed prevent the occurrence of premature breakup of drops and ligaments from the liquid sheet thereby improving the statistics of atomization however incurring high computational cost. The next observation can be seen as the multi-modality of the PDF of DSD from the simulations for both the Fp (c_1^{Fp}) and Cp (c_2^{Cp}) inlet velocity profile cases which is in agreement to the profile of the experimental data. Although, the profiles of the Fp and Cp simulation cases overlap approximately (especially for the small diameter values), there seems to be a non-negligible effect on the atomization characteristics by the change in the inlet velocity profile. For example, the Cp case is yielding relatively higher probability of occurrence of large sized drops than in the Fp case. To present a more quantitative comparison, the first and second peaks from the experimental data are located at 35.5 µm and 63.5 µm respectively and that of the Fp (c_1^{Fp}) case are located at 29.20 µm and 68.14 µm while for the Cp (c_2^{Cp}) case are located at 32.39 µm and 63.16 µm. Therefore, we can see that the profile of DSD from the simulations are following that of the experiments with the first two dominant peaks located around the same diameter value as that of the experiments.

Another important atomization characteristic that define the quality of injection along with the DSD is the Sauter Mean Diameter (SMD). This quantity is computed from the experimental and simulation data using the expression

$$\text{SMD} = \frac{\int \text{PDF}(D) D^3 dD}{\int \text{PDF}(D) D^2 dD}; \quad D = d_{\text{drop}}. \tag{14}$$

The SMD computed from the experiments is 154.80 µm and the Fp (c_1^{Fp}) simulation case is 130.13 µm and the Cp (c_2^{Cp}) simulation case is 150.37 µm. First, it can be observed that the SMD values from the simulations are of the same order of magnitude as that of the experiments. Second, the SMD of the Cp simulation case is having an excellent agreement with the experiments indicating that the channel flow velocity profile for the gas with a linear velocity profile for the liquid representing a more physical velocity profile. However, an

obvious question now is that, if the profiles of the Fp and Cp simulation cases are qualitatively overlapping, how can their SMD values differ? To answer this question, it is to be remarked that the SMD is highly sensitive to the presence of drops with large diameter values. As can be seen in Figure 14, the Cp case is yielding relatively higher probability for the large drops than that of the Fp case albeit their qualitative profile matching for the smaller diameters.

Overall, there is a satisfactory agreement between the simulations and experiments with the profile and trend of the curves of PDF of DSD from simulations following the experiments. Furthermore, the PDF values are in the same order of magnitude as that of the experiments while an under-prediction is observed quantitatively.

4.2.2. Drop velocity distribution

The drop velocity distribution (DVD) is an another important quantity along with the DSD that is useful for the subsequent Lagrangian and Eulerian simulations for primary and secondary atomization modeling. The PDF of the DVD is constructed in the same manner as that of the DSD from the simulations. As part of the connected component labelling (CCL) structure detection algorithm [68], we extract the volume-weighted averaged velocity of the centroid of each liquid structure weighted by the total liquid volume of the structure. After the sampling of the drops at the $z = 6.6\,\text{mm}$ plane, the streamwise component (i.e., w_z component) of the drop velocity is binned to form the PDF of the DVD.

Figure 15 shows the PDF of the DVD for the streamwise component of the droplet velocity. First, it can be seen that the results from the simulation for both the flat profile and channel profile cases are agreeing very well with the experimental data. Second, the simulation is quantitatively over-predicting the probability of drop velocity in comparison to the experiments. Third, the peak value of the DVD from the simulations are agreeing very well with the simulations, although the curve for the c_2^{Cp} case is shifted towards a lower velocity value. Finally, there is an observed effect of the change of inlet velocity profile from flat profile to channel profile resulting in a wider distribution of velocity and the peak of the PDF curve occur at a lower value of drop velocity $w_{z_{\text{drop}}}$. This is because the shear near the liquid film is larger with a flat velocity profile and as a consequence the slip velocity between liquid and gas phase becomes large resulting in larger drop velocities. In summary, inlet velocity profile does have an effect on the DVD of the liquid in the simulations and an overall good agreement between the simulations and the experiments is observed.

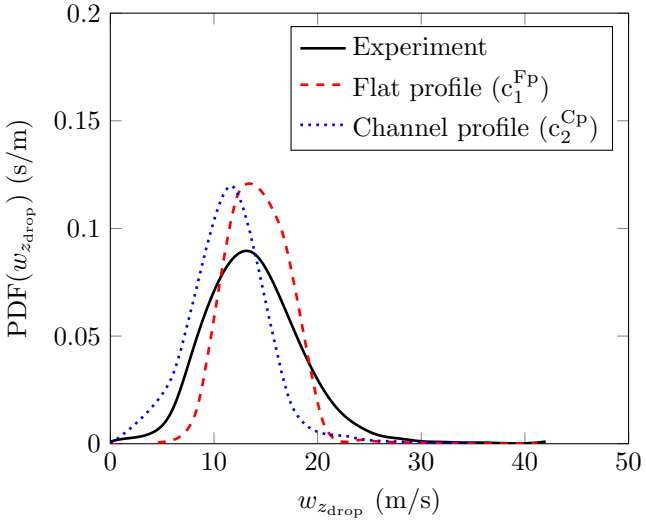

Figure 15: Plot of drop velocity distribution (DSD) for flat profile (Fp) c_1^{Fp} (- - -) and channel profile (Cp) c_1^{Cp} (·····) inlet profile cases from the simulations along with experimental data [16] (——).

4.2.3. Secondary atomization

Many of the previous studies on experimental [12, 13, 14, 15] and numerical [16, 17, 18, 19] investigations of Airblast atomization of liquid sheet have focused entirely on the primary atomization. However, it is physically and statistically possible that the atomized drops produced from various breakup mechanisms can undergo secondary atomization within the computational domain under investigation. The data about the presence of secondary atomization for Airblast atomization will be directly helpful for the secondary breakup modeling (SBM) that focuses on developing breakup models based on aerodynamic forces and turbulence. In order to investigate the existence of the secondary atomization of the drops in this work, we have computed the PDF of the DSD at various downstream locations (i.e., along the $z-$direction) as shown in Figure 16 for both the flat profile and channel profile simulation cases. From these plots, we can see that PDF curves do not collapse into a single curve for both these cases for any of the sampling location. Moreover, the peaks of the PDF curves keep shifting towards the higher drop diameter d_{drop} values. This is an indication towards the drop coalescence, i.e., smaller drops aggregate forming a bigger drop. From these inferences, it can be concluded that there is lower probability of occurrence of secondary atomization however, higher probability of drop coalescence.

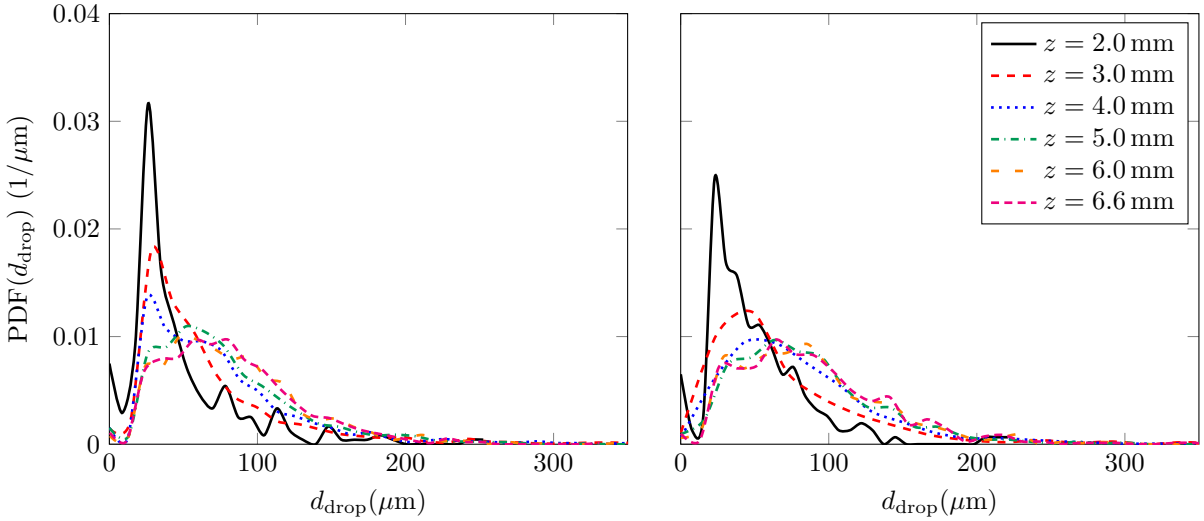

(a) Flat profile (Fp) c_1^{Fp} case

(b) Channel profile (Cp) c_2^{Cp} case

Figure 16: PDF of DSD sampled at various downstream locations of $z = 2\,\text{mm}$ (——), $3\,\text{mm}$ (- - -), $4\,\text{mm}$ (·····), $5\,\text{mm}$ (-·-·-), $6\,\text{mm}$ (- -), $6.6\,\text{mm}$ (----) from flat profile (Fp) c_1^{Fp} and channel profile (Cp) c_2^{Cp} simulation cases.

In order to investigate further into the change in the peaks of the PDF curves, we have shown in Figure 17 the plots of the evolution of the number based frequency distribution of the drop diameters. This plot, unlike the PDF plot, is devoid of the constraint to keep the area under the curve equal to unity which changes the location of the peak of the PDF. Hence, from these plots, it is possible to make a convincing argument towards the evolution of the drop diameters in the downstream direction. It can be seen that frequency distribution curves measured at various downstream locations do not collapse. Moreover, it can be inferred that peak of these curves indeed move towards the higher drop diameter values when the sampling location changes. Furthermore, we can see that the number of larger drops downstream are increasing while there is a simultaneous decrease in the number of small drops indicating the occurrence of phenomenon of drop coalescence. That being concluded, there is a non-negligible probability of occurrence of secondary atomization in the simulations since decrease of the number of small sized drops is not by an order of magnitude smaller between the sampling locations.

To make a conclusive argument about the presence of secondary atomization and drop coalescence, we now show the plots of the evolution of the Sauter Mean Diameter (SMD) measured at the different

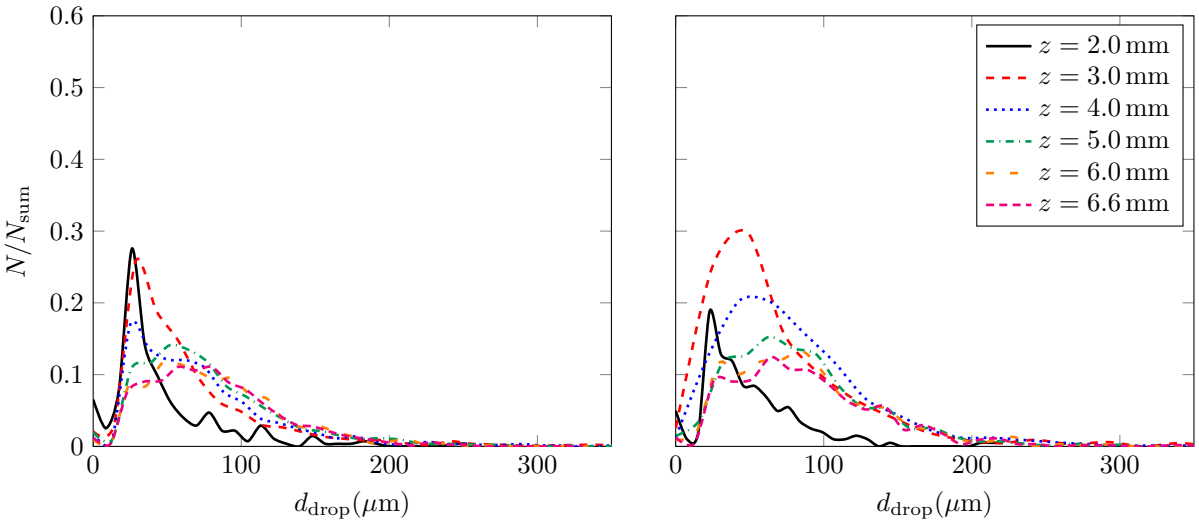

(a) Flat profile (Fp) c_1^{Fp} case

(b) Channel profile (Cp) c_2^{Cp} case

Figure 17: Number based frequency distribution of drop diameter sampled at various downstream locations of $z = 2\,\text{mm}$ (——), 3 mm (- - -), 4 mm (·····), 5 mm (-·-·-), 6 mm (- -), 6.6 mm (-·-·-) from flat profile (Fp) c_1^{Fp} and channel profile (Cp) c_2^{Cp} simulation cases.

downstream sampling locations. The SMD values at various downstream sampling locations are computed using the Equation (14). There is an observed increase in the SMD values along the downstream between $z = 1.5\,\text{mm}$ to $z = 3\,\text{mm}$ after which there is an observed decrease. The increase in the SMD could be attributed to the formation of large number of small sized drops that are ejected from the accumulated liquid in the pre-filmer plate. The subsequent decrease could be attributed to the drop coalescence leading to the formation of larger drops. The choice of the inlet velocity profile for the liquid and gas does seem to have an effect on the value of the peak of the evolution of the SMD of the drops. Hence, from these inferences, it can be concluded that there is equal probability of secondary atomization and drop coalescence in the computational domain.

Finally, to validate the occurrence of the secondary atomization of drops, we have computed an approximate drop-based Weber number according to

$$\text{We}_{\text{drop}} = \frac{\rho_{\text{gas}}(w_{\text{gas}} - w_{z_{\text{drop}}})^2 d_{\text{drop}}}{\sigma}. \tag{15}$$

A scatter plot of the drop velocity and drop diameter colored by We_{drop} for all the sampled drops collected (counted once) from various sampling locations is shown in Figure 19.

On observing the scatter plot, it can be seen that there are large number of drops with a velocity around 8 m/s for all the investigated cases. Moreover, a number of small sized drops (located in the downstream of the domain) with a high velocity are found. These drops attain very high velocity mainly due to their low Stokes number thereby being carried away with the gas phase flowing at a speed of 50 m/s. Furthermore, it can be found that large droplets with velocities between 0 m/s and 10 m/s. These large drops (or liquid structures) are part of the liquid film injected on the pre-filmer plate and have no significant influence on the DSD and DVD that are computed solely for the atomized drops. It can be seen that the inlet velocity does not seem to have an effect on the distribution of the drop diameter and velocity.

From the point of view of secondary atomization, it can be seen that the large drops have higher Weber number than the small drops due to their low velocity thereby causing the $w_{\text{gas}} - w_{z_{\text{drop}}}$ to be high eventually resulting in high Weber number. Another striking observation from the plots is that the Weber number is approximately a linear function of the drop diameter since the value of the former changes almost linearly

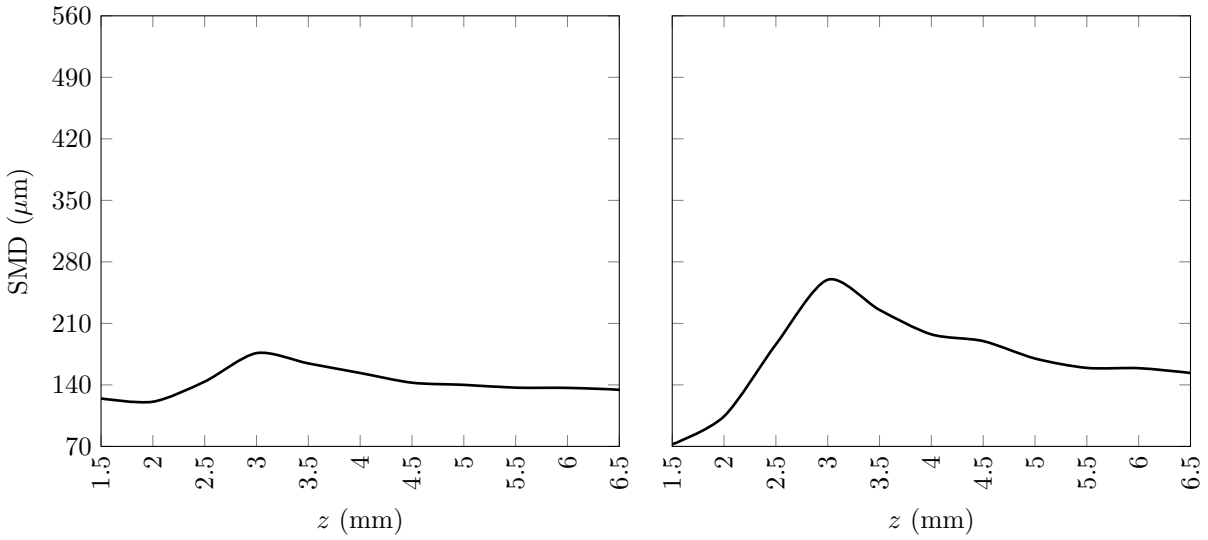

(a) Flat profile (Fp) c_1^{Fp} case

(b) Channel profile (Cp) c_2^{Cp} case

Figure 18: Evolution of Sauter Mean Diameter (SMD) of drops along downstream direction for flat profile (Fp) c_1^{Fp} and channel profile (Cp) c_2^{Cp} simulation cases.

with the latter. This goes to show that the drops are sampled within a small domain as soon as the primary atomization event occurred. One of the ways to mitigate this problem is to consider a larger computational domain in the simulations for the same or higher mesh resolution to capture the breakup physics. Another way to resolve this issue is to increase the mesh resolution but this approach will increase the computational cost multi-fold. According to Pilch and Erdman [69], drops with Weber number We < 12 will experience no secondary atomization due to aerodynamic forces while the drops with Weber number in the range $12 \leq$ We ≤ 50 experience further atomization due to bag breakup mechanism. We found that about 38% and 45% of the total number of drops are having We ≤ 12 for the flat profile (Fp) and the channel profile (Cp) cases respectively. Since majority of the drops are having We > 12 , it can be concluded that there will be higher probability of occurrence of secondary atomization in the computational domain for both the inlet velocity profile cases. In summary, there is evidence of occurrence of both secondary atomization as well drop coalescence in the simulations for both the flat profile and channel flow inlet velocity profile cases of the simulations.

4.3. Ligament analysis

Aside from the sheet breakup mechanism, the ligament breakup mechanism is one of the dominant atomization mechanism for the drop formation in planar pre-filming Airblast atomization process. The liquid ligaments are formed at the trailing edge of the pre-filmer plate (refer Figure 1) predominantly as shown in Figure 12. They are then stretched to their limit due to the aerodynamic forces from the high speed gas flowing above and below the pre-filmer plate and then breakup into droplets. In the past studies, the quantitative data extracted from the simulations [17, 18] and experimental measurements [23, 22] pertain mainly to the far downstream quantities such as DSD and DVD. In a recent study [14], the data in the near-field region of the injector pertaining to liquid ligaments have been extracted. Such near-field primary breakup data are immensely useful for understanding the physics of atomization. The study by Warncke et al. [16] coupled the experimental and numerical work on the analysis of the near-field ligament data extracted from the experiments and simulations.

As part of the analysis of these extracted ligaments in this work, we computed their breakup lengths and associated breakup velocities using which the breakup frequency can be obtained. This frequency is loosely connected to the flapping frequency of the liquid sheet which when known is useful in studying the

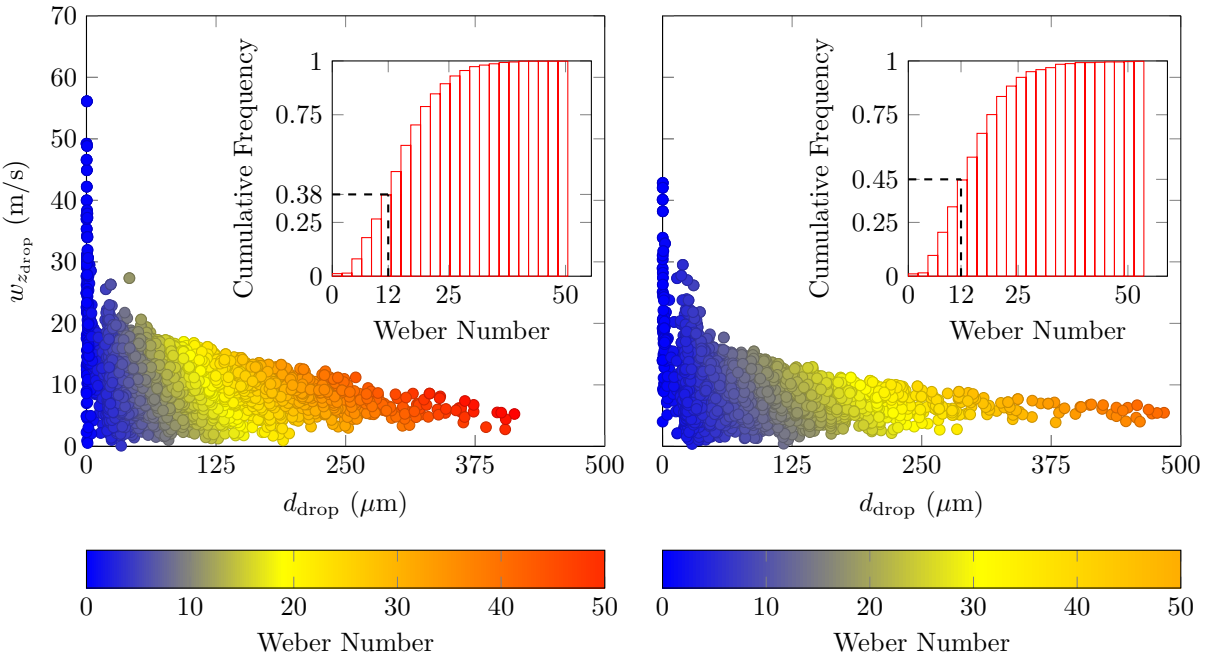

(a) Flat profile (Fp) c_1^{Fp} case

(b) Channel profile (Cp) c_2^{Cp} case

Figure 19: Scatter plot of drop diameter d_{drop} and streamwise component of drop velocity $w_{z_{\text{drop}}}$ colored by drop-based Weber number (We) for flat profile (Fp) c_1^{Fp} and channel profile (Cp) c_2^{Cp} simulation cases.

dynamics of liquid atomization. The following subsections present the procedure and the methodology of computation of the ligament breakup length and ligament breakup velocity in the near-field region of the pre-filmer plate (i.e., the Airblast atomizing injector).

4.3.1. Ligament breakup length

As part of the near-field data extraction, we first compute the breakup length of the ligaments. To that end, it is imperative to first detect and identify the ligaments from the accumulated liquid at the trailing edge of the pre-filmer plate. We first present the procedure [16] to identify the ligaments and compute their lengths. The length of a ligament l_{lig} is defined as the distance between the edge of the pre-filmer plate and the tip of the liquid structure (from the accumulated liquid) extended in the downstream direction as shown in Figure 20.

The identification and extraction of ligament length from the accumulated liquid in the pre-filmer plate edge is challenging. This is because the interface at the trailing edge experiences high shear and aerodynamic forces making it difficult to distinguish between interface wrinkle and a liquid ligament. To mitigate this issue, we have used a ligament detection algorithm [16] that is split into four steps [70, 71, 72]. First, the 3D simulation data (c.f. Figure 21a) is reduced to a 2D data that is analogous to the shadowgraphy images (from experiments) by assigning label value of 0 (for gas) and 1 (for liquid) to each cell with zero and non-zero liquid volume fraction respectively. Second, these label values are summed up along cross-stream $x-$direction to generate a projected top view ($y-z$ plane view) (c.f. Figure 21b). Any cell in this top view with a summed label value greater than 1 indicates presence of liquid in this view. Third, a connected component labelling (CCL) algorithm [68] is applied for these summed up label values to identify the biggest liquid structure which forms the accumulated liquid at the trailing edge of pre-filmer plate (c.f. Figure 21c). Finally, the 1D interface contour that characterizes the interface of this accumulated liquid is identified using the method described in Ref. [73, 74] (c.f. Figure 21d). This procedure has been applied to every sampled time step (simulation data written to disk approximately every 35 µs of physical time) since the first breakup

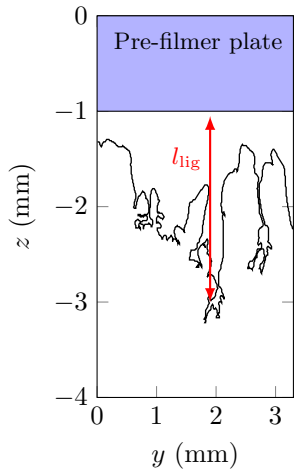

Figure 20: Measurement of ligament length (l_{lig}) from the trailing edge of pre-filmer plate.

event has occurred in the simulations. An example of a time step to which this four step algorithm is shown in Figure 21.

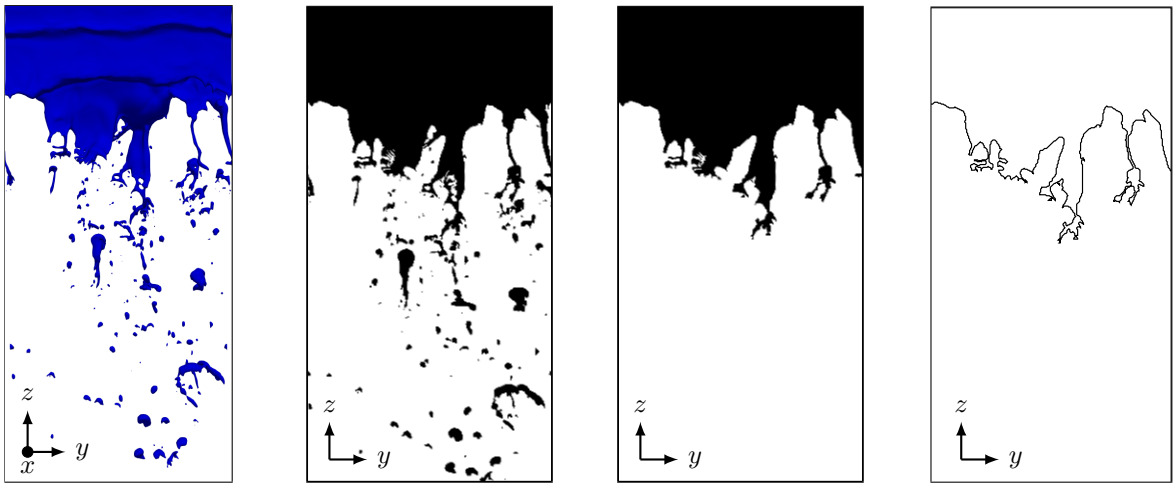

(a) 3D data (b) 2D Projected data (c) Accumulated liquid (d) 1D interface

Figure 21: Reduction of 3D to 1D data for computing ligament characteristics for $t = 5.05\,\text{ms}$ for the case $\text{c}_{11,\text{F}_\text{P}}^{\text{CLSVOF}}$.

The length of the ligament is the computed using the 1D interface contour obtained from the reduction algorithm. The maximum dip in this 1D phase interface along the downstream $z-$direction is used for identifying the ligaments. In order to identify these dips in the interface, we have used a technique to traverse through the 1D contour finding the local maxima (dips) and local minima (rises) with the direction of the dip pointing towards the downstream direction. This is shown in Figure 22 in which the blue solid square indicate the location of local maxima and red hollow circles indicate the location of local minima. The distance of the local maximum dips can be considered a starting point in computing the length of the ligaments. The critical step in this computation is to eliminate the effect of the wrinkling in the interface. To that end, we have employed a technique, following Warncke et al. [16], in which the local maximum dips are eliminated from the list of maximum dips when the streamwise distance (measured along $z-$direction) between adjacent local maximum dips and local maximum rise is less than $50\,\mu\text{m}$. It is to be remarked

that the choice of this threshold is arbitrary and the value of 50 µm is chosen following Warncke et al. [16] such that there is a balance between the elimination of interface wrinkle and the detection of physical liquid ligaments. The remaining local maxima after the filtering process become the liquid ligaments and their length is considered as ligament length l_{lig}.

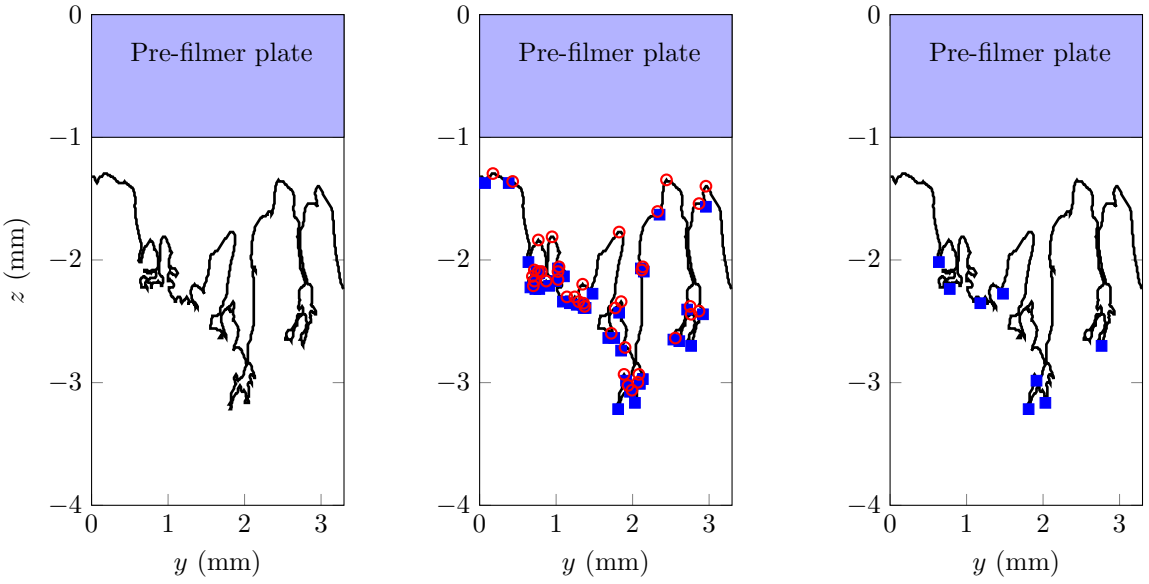

(a) 1D interface contour (b) Local maxima and minima (c) Filtered maxima

Figure 22: Detection and filtering of the local maxima in the 1D interface contour for ligament length computation with local maxima (■) and local minima (○).

The ligament breakup length $L_{\text{lig}}^{\text{breakup}}$ is then computed as the *mean* of all ligament lengths over all sampled time steps from the simulations, i.e.,

$$L_{\text{lig}}^{\text{breakup}} = \frac{\sum_{i=1}^{N} l_{\text{lig}_i}}{N}, \tag{16}$$

where N is the total number of sampled ligaments (i.e., total number of filtered maxima collected over all sampled time steps). Using this expression, the ligament breakup length from the simulations is determined to be 1.32 mm for the flat profile (Fp) c_1^{Fp} case and 1.55 mm for channel profile (Cp) $c_{2,\text{Cp}}$ case. However, the value of the ligament breakup length measured from the experiments [16] is 3.2 mm. The under-prediction in the simulations can be partly attributed to the fact that the size of the domain investigated in the experiments is much larger than the simulations and ligaments longer than the streamwise direction length of the simulation domain are found in the experiments. To characterize the overall spread of the size of these sampled ligaments, a frequency distribution of the ligament lengths is presented in Figure 23. The maximum measurable length from the simulation is $l_{\text{lig}}^{\text{max}} = L - l_{\text{pf}} = 5.6$ mm (since the ligament length is measured from the edge of pre-filmer plate) is also marked in this figure. From this plot, it can be seen that a small number of ligaments of the size larger than the streamwise domain length (6.6 mm) are detected in the experiments. The simulation results are found to under-predict the length of the liquid ligaments since the peak of the frequency distribution is shifted towards smaller ligament lengths. It is however noteworthy to point out that the channel profile (Cp) c_2^{Cp} is agreeing relatively well with the experimental data compared to the flat profile (Fp) c_1^{Fp} case. This under-prediction could be attributed to under-resolution in the simulations to capture the breakup events. Such an under-resolution often leads to premature breakup of the ligaments from the accumulated liquid structure resulting in smaller value of the sampled ligament lengths. The

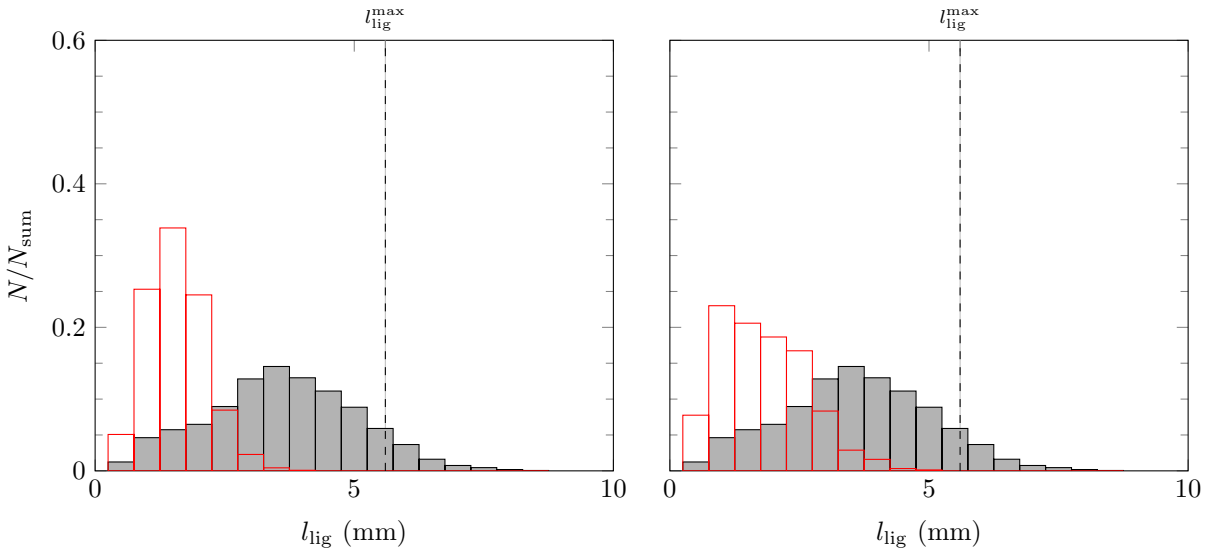

(a) Flat profile (Fp) c_1^{Fp} case

(b) Channel profile (Cp) c_2^{Cp} case

Figure 23: Plots of frequency distributions of the ligament lengths between experiment (▭) and simulations (▭) for flat profile (Fp) and channel profile (Cp) cases. The maximum measurable ligament length in the computational domain $l_{\text{lig}}^{\max} = 5.6\,\text{mm}$ is marked in the plot using dashed line.

maximum ligament length measured from the experiments is 8.75 mm while that from the simulations are 3.75 mm for the flat profile (Fp) c_1^{Fp} case and 4.75 mm for the channel profile (Cp) c_2^{Cp} case. This could be attributed to multiple reasons: first, no ligament sampled from our simulations reaches the outlet of the domain (i.e., maximum ligament length measured is less than streamwise domain length); second, there was greater time period for the sampling in the experiments, and therefore, a higher amount of samples compared to the simulations; and finally, the field of view of measurement for experiments are larger than that of the simulations, thus, longer ligament lengths that are greater than the length of the streamwise direction of the computational domain are observed. In summary, it can be concluded that the ligament breakup length obtained from the simulations are of the same order of magnitude as that of the experiments and a satisfactory agreement between the simulations and experiments is observed.

4.3.2. Ligament breakup velocity

As a final quantitative analysis of the atomization characteristics, the velocity of the ligaments w_{lig} at the trailing edge of the pre-filmer plate is computed. The rationale behind computing this quantity is to subsequently compute the ligament breakup frequency which can potentially give an idea towards the rate of atomization/breakup. The breakup frequency is a vital quantity in identifying and isolating the study into ligament based breakup mechanism.

To that end, we employ a technique [16] exploiting the displacement of the interface of the 1D contour of the accumulated liquid between adjacent sampled time steps from the simulations (similar to the experimental measurements) to compute the ligament velocity. Such a technique is employed to determine the ligament breakup velocity from the simulations in order to have a consistent comparison with the experimental data. The procedure to obtain the velocity of the identified ligaments (i.e., all filtered maxima from the 1D interface contour) is as follows. Due to the interface wrinkling, it is challenging to identify a single point on the 1D interface contour (see Figure 21d) using which ligament velocity between adjacent time steps can be computed (see Figure 24). Moreover, the ligaments are stripped throughout the width of the pre-filmer plate, thus, choosing one point for the computation of ligament velocity would not be a complete description and not be representative of the ligament breakup velocity. Therefore, in order to overcome this challenge, a simplified calculation is performed in which we determine the displacement of the

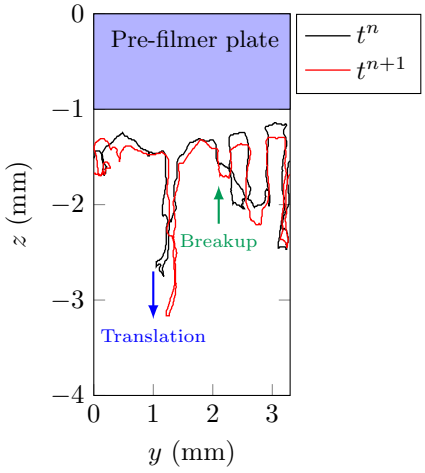

Figure 24: Displacement of interface.

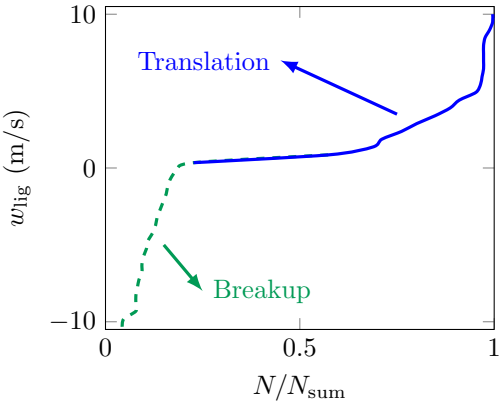

Figure 25: Cumulative distribution of w_{lig} for two consecutive sampled time steps.

1D interface contour by finding the most remote point (along the downstream $z-$direction) $z_{\max}$ for each point in the spanwise $y-$direction between the adjacent time steps t^n and t^{n+1}. The ligament velocity along the streamwise direction is then computed as

$$w_{\text{lig}_j} = \frac{z_{\max,y_j}(t^{n+1}) - z_{\max,y_j}(t^n)}{t^{n+1} - t^n} \quad \forall\ j = 1, 2 \ldots N_y, \tag{17}$$

where N_y is the total number of grid points along the $y-$direction in the computational domain in the simulations. Now, the obvious question is, which velocity on the point y_j need to be considered as the ligament velocity? To answer that question, we compute a cumulative frequency distribution of the computed ligament velocity shown in Figure 25 for a consecutive sampled time step pair (t_1, t_2). The negative velocities (shown by green dashed line in this figure) represent the breakup of the ligaments while the positive velocities (shown by blue solid line) represent the translation/advection of the ligaments. The study by Warncke et al. [16] had taken the 90%-quantile from this distribution as the representative velocity of the ligaments. However, in this work, the ligament velocities are computed for three different quantiles – 90%-, 95%-, and 99.75%-quantiles. The rationale behind this approach is to demonstrate the dependence of the ligament velocity on the selection of quantile. For the sake of the simplicity in notation, each quantile is represented by q where $q = 90, 95, 99.75$ for the remainder of this subsection. An exemplary depiction of the computation of the 90%-quantile velocity w_{lig}^{90} from the cumulative distribution is shown in Figure 25. The 95%-quantile velocity w_{lig}^{95} and 99.75%-quantile velocity $w_{\text{lig}}^{99.75}$ are computed in the same manner from the cumulative distribution. The mean value of this quantile velocity w_{lig}^{90} is considered to be the breakup velocity of the ligaments for the current operating point of the pre-filming planar Airblast atomization, i.e.,

$$w_{\text{lig}}^{\text{breakup},q} = \frac{\sum_{i=1}^{N} w_{\text{lig}}^{q}}{N}, \tag{18}$$

where N is the number of sampled consecutive time step pairs from the simulations and $q = 90, 95, 99.75$ which is not an exponent.

Based on this expression, the ligament breakup velocity $w_{\text{lig}}^{\text{breakup},90}$ along the streamwise direction from the simulations are determined to be 2.48 m/s for the flat profile c_1^{Fp} case and 2.16 m/s for channel profile (Cp) c_2^{Cp} case. Similarly, the computation of the ligament breakup velocity for 95%-quantile $w_{\text{lig}}^{\text{breakup},95}$ yield 4.06 m/s for the flat profile c_1^{Fp} case and 3.06 m/s for channel profile (Cp) c_2^{Cp} case. Finally, the computation

using the 99.75%-quantile yield 17.72 m/s for the flat profile c_1^{Fp} case and 9.00 m/s for channel profile (Cp) c_2^{Cp} case. The ligament breakup/deformation velocity from the experiments is determined to be 15.7 m/s [16]. A number based frequency distribution of the 90%-quantile of the ligament velocities w_{lig}^{90}, w_{lig}^{95}, $w_{lig}^{99.75}$ are presented in Figures 26 to 28 shedding light on the spread of the ligament velocity. From this plot, it can be seen that the simulation results are under-predicting the experimental data for the ligament velocities computed using 90%-quantiles while having satisfactory agreement for the 95%-quantile and having excellent agreement for the 99.75%-quantile. For the case of the 90%-quantiled ligament velocity, the results from the simulation predicts towards the presence of large number of ligaments with low velocities potentially pointing towards the improvement to be made in the simulation towards the direction of larger sampling time or larger number of samples required. A higher mesh resolution could definitely be helpful in obtaining larger ligament velocity due to the fact that they would support the existence of longer, thinner ligaments (preventing numerically induced artificial breakup) which could be accelerated by the high speed gas stream for longer times reaching higher velocities. Moreover, these observed high number based frequencies for small ligament velocity values could be attributed to the large sampling time between consecutive sampled time instants from the simulations. In this work, we have sampled every 35 µs which is chosen based on the existing available computational resources [58]. Now, it is expected that within this sampling time, numerous breakup events occur leading to changes in the shape of the accumulated liquid occurring at the trailing edge of the pre-filmer plate which could have an effect on the ligament velocity computation. However, results pertaining to the 95%-quantiled and the 99.75%-quantile demonstrate and emphasize that the simulations presented in this work are yielding physically close agreement with the experimental measurements while a mesh resolution improvement can definitely be beneficial.

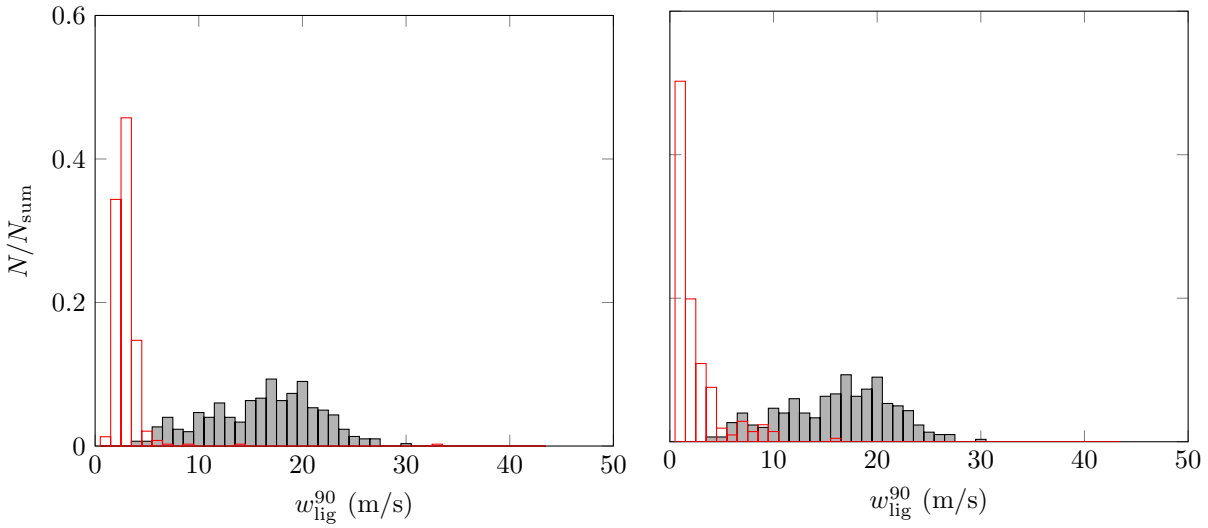

(a) Flat profile (Fp) c_1^{Fp} case

(b) Channel profile (Cp) c_2^{Cp} case

Figure 26: Plots of frequency distribution of the ligament velocity from experiment (▭) and simulations (▭) for 90%-quantile ligament velocity.

The global liquid sheet oscillation frequency is challenging to be determined as there is no continuous flapping sheet behind the trailing edge of the pre-filmer plate. Alternatively, mean breakup frequency [16] could be loosely coupled with the frequency of the flapping of the liquid sheet. This frequency is computed as a measure of the time distance between consecutive events of atomization. The mean breakup frequency ($f^{breakup}$) is computed using the ligament breakup length and its velocity using the following expression,

$$f^{breakup} = \frac{L_{lig}^{breakup}}{w_{lig}^{breakup}}. \tag{19}$$

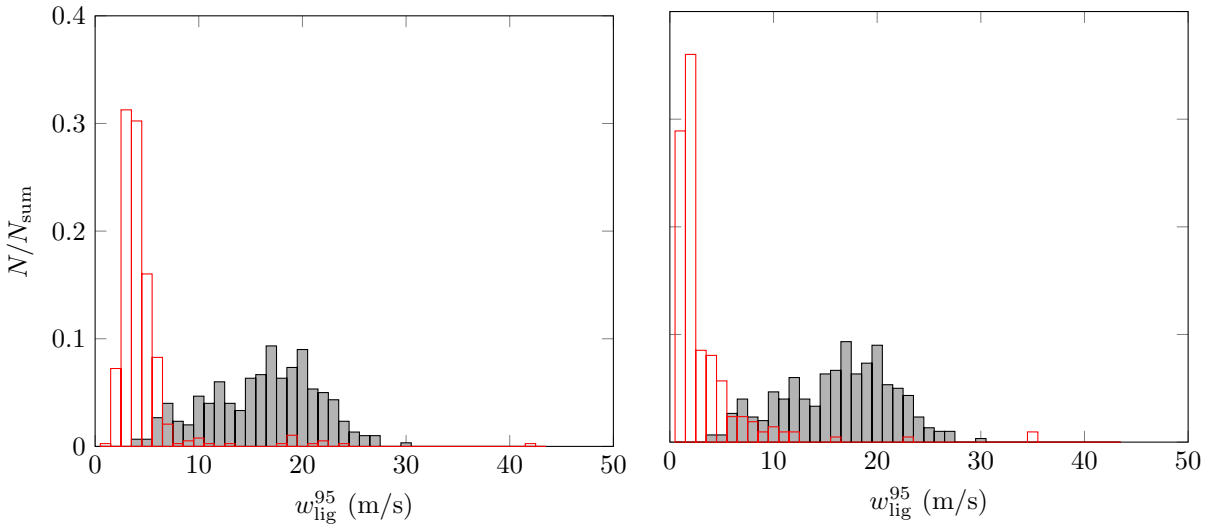

(a) Flat profile (Fp) c_1^{Fp} case

(b) Channel profile (Cp) c_2^{Cp} case

Figure 27: Plots of frequency distribution of the ligament velocity from experiment ( ) and simulations ( ) for 95%-quantile ligament velocity.

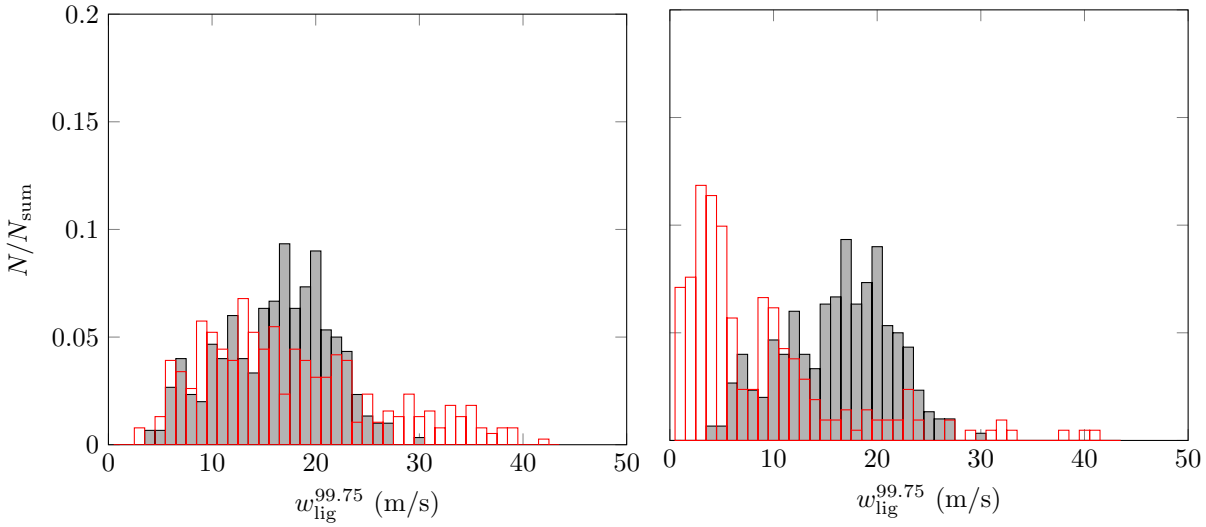

(a) Flat profile (Fp) c_1^{Fp} case

(b) Channel profile (Cp) c_2^{Cp} case

Figure 28: Plots of frequency distribution of the ligament velocity from experiment ( ) and simulations ( ) for 99.75%-quantile ligament velocity.

This frequency is computed for each quantiled ligament velocity in the simulations and is determined to be 1878.79 Hz for the flat profile (Fp) c_1^{Fp} case and 1393.56 Hz for the channel profile (Cp) c_2^{Cp} case for 90%-quantiled ligament velocity, 3075.76 Hz for the flat profile (Fp) c_1^{Fp} case and 1974.19 Hz for the channel profile (Cp) c_2^{Cp} case for 95%-quantiled ligament velocity, and 13,424.24 Hz for the flat profile (Fp) c_1^{Fp} case and 5806.45 Hz for the channel profile (Cp) c_2^{Cp} case for 99.75%-quantiled ligament velocity while the value from the experiments [16] is determined as 4906.25 Hz. It can be seen that the simulation results are under-predicting the experimental value for the 90%- and 95% quantiles while over-predicting for the

99.75%-quantile value. Nevertheless, the breakup frequency obtained from the simulation are of the same order of magnitude as the experiments except for the 99.75%-quantiled ligament velocity for the flat profile (Fp) c_1^{Fp} case. Finally, the results presented in this subsection regarding the near-field data of the ligaments are summarized in Table 6.

Table 6: Summary of ligament characteristics from the experiments and simulations (flat profile (Fp) and channel profile (Cp)).

Quantities	**Experiments** [16]	**Simulations**					
		Flat profile (Fp)			Channel profile (Cp)		
		w_{lig}^{90}	w_{lig}^{95}	$w_{\mathrm{lig}}^{99.75}$	w_{lig}^{90}	w_{lig}^{95}	$w_{\mathrm{lig}}^{99.75}$
Breakup velocity ($w_{\mathrm{lig}}^{\mathrm{breakup}}$) [m/s]	15.7	2.48	4.06	17.72	2.16	3.06	9.00
Breakup length ($L_{\mathrm{lig}}^{\mathrm{breakup}}$) [mm]	3.20		1.32			1.55	
Breakup frequency (f^{breakup}) [Hz]	4906.25	1878.79	3075.76	13424.24	1393.56	1974.19	5806.45

5. Conclusions

Results from the detailed numerical simulations of planar pre-filming Airblast atomization have been presented. The simulations have been performed for an aircraft altitude relight operating condition using hybrid moment of fluid–level set (HyMOFLS) method of liquid/gas interface reconstruction within the context of multiphase flows. The geometry of the annular atomizer is reduced to a planar pre-filming configuration with the rationale of direct and consistent comparison of the simulation results with the experimental data and easy generation of inlet boundary conditions in the simulations. In order to find the effect of inlet velocity profile for the liquid fuel and gaseous air, two different velocity profiles have been used – flat velocity profile for the liquid and gas phase and linear velocity profile for liquid phase with turbulent channel flow velocity profile for the gas phase. The turbulence in the simulations have been generated in the gas phase using synthetic turbulence method.

The interface visualizations realized from the simulations show that the overall atomization process comprises of the high speed air destabilizing the liquid fuel film/sheet injected on the solid pre-filmer plate resulting in accumulation of the liquid at the trailing edge of the plate. This accumulated liquid either forms bag-like structure which then breaks up into droplets or formation of ligaments at the plate edge which disintegrates into droplets. The bag/sheet breakup mechanism and ligament breakup mechanism have been observed to be the two predominant breakup mechanisms driving the Airblast atomization for this configuration. The former breakup mechanism often produces droplets that are of the size of the thickness of the sheet while the latter mechanism produces droplets of the size of the ligament diameter which is usually larger than the bag/sheet thickness. Such a combination of breakup mechanism has been found to be consistent with the experimental observations. The quantitative comparison of the drop size distribution (DSD) and drop velocity distribution (DVD) between simulations and experiments showed that the simulation results are of the same magnitude as that of the experimental results however, under-predicting quantitatively. Moreover, the Sauter Mean Diameter (SMD) determined from the simulations are having excellent agreement with the experiments. As a novel analysis, the near-field atomization characteristics pertaining to the liquid ligaments have been extracted from the simulations. The attributes of the ligaments extracted include their breakup length and associated breakup velocity. The ligament lengths from the simulations have been observed to be of the same order of magnitude as that of the experiments although their frequency distributions are under-predicted. The ligament velocity computed from the simulations

have been observed to be under-predicting the experimental data although of the same order of magnitude as the experimental data. This could be attributed to the long measurement time and the large domain size in the experiments as that used in the simulations. In summary, the ability to simulate such a high shear atomization mechanism by the HyMOFLS method has been demonstrated; and, a satisfactory agreement has been achieved between the simulations and experimental results for the Airblast atomization phenomenon.

One of the many directions to improve the results from the simulations is through adaptive mesh refinement (AMR) which would be beneficial to capture the local atomization events and capture the breakup physics through local mesh refinement. New developments are planned towards implementation of AMR strategy to analyze the physics of the breakup and instability waves formed on the liquid sheet.

Acknowledgements

The funding for this project from the European Union's Horizon 2020 research and innovation programme under the Marie Skłodowska-Curie grant agreement N° 675676 is gratefully acknowledged. The authors would like to thank Prof. Dr. Jean-Bernard Blaisot for graciously sharing the algorithm of finding the 1D interface contour. The authors wish to thank Prof. Rainer Koch and his group at Institut für Thermische Strömungsmaschinen in Karlsruher Institut für Technologie (KIT), Germany for graciously sharing their experimental data. Anirudh Asuri Mukundan express gratitude to Dr. Fabien Thiesset for blender image rendering tutorial and beginner scripts and to Dr. Ruud Eggels and Dr. Max Staufer for many fruitful discussions. The computing time at CRIANN (Centre Régional Informatique et d'Applications Numériques de Normandie) under the scientific project No. 2003008 and at GENCI-[TGCC/CINES/IDRIS] (Grant2019-2613) are also gratefully acknowledged.

References

[1] Current Market Outlook 2019–2038, Technical Report, Boeing, 2019.
[2] Airbus Global Market Forecast 2019–2038, Technical Report, Airbus, 2019.
[3] V. McDonell, Lean Combustion, second edition ed., Academic Press, 2016, pp. 147–201. URL: https://doi.org/10.1016/B978-0-12-804557-2.00005-5. doi:10.1016/B978-0-12-804557-2.00005-5.
[4] A. H. Lefebvre, D. Miller, The development of an Air Blast Atomizer for gas turbine application, Technical Report CoA Report AERO No. 193, The College of Aeronautics Cranfield, 1966.
[5] J. C. Lasheras, E. Villermaux, E. J. Hopfinger, Break-up and atomization of a round water jet by a high-speed annular air jet, Journal of Fluid Mechanics 357 (1998) 351–379. URL: https://doi.org/10.1017/S0022112097008070. doi:10.1017/S0022112097008070.
[6] E. Villermaux, Mixing and spray formation in coaxial jets, Journal of Propulsion and Power 14 (1998) 807–817. doi:10.2514/2.5344.
[7] P. Marmottant, E. Villermaux, On spray formation, Journal of Fluid Mechanics 498 (2004) 73–111. URL: https://doi.org/10.1017/S0022112003006529. doi:10.1017/S0022112003006529.
[8] R. Chiodi, G. Agbaglah, O. Desjardins, Validation and analysis of air-blast atomization simulations, in: Proceedings of the ILASS Americas, 28th Annual Conference on Liquid Atomization and Spray Systems, May 15-18, Dearborn, MI, USA, 2016.
[9] R. Chiodi, O. Desjardins, A numerical parametric study on the air-blast atomization of a planar liquid layer, in: Proceedings of the 55th AIAA Aerospace Sciences Meeting, January 9-13, Grapvine, TX, USA, 2017. URL: https://doi.org/10.2514/6.2017-1702. doi:10.2514/6.2017-1702.
[10] R. Chiodi, O. Desjardins, An exploration of initial destabilization during air-blast atomization using 3d simulations, in: Proceedings of the ILASS Americas 29th Annual Conference on Liquid Atomization and Spray Systems, May 15-18, Atlanta, GA, USA, 2017.
[11] M. Owkes, O. Desjardins, A mass and momentum conserving unsplit semi-Lagrangian framework for simulating multiphase flows, Journal of Computational Physics 332 (2017) 21–46. URL: https://doi.org/10.1016/j.jcp.2016.11.046. doi:10.1016/j.jcp.2016.11.046.
[12] U. C. Bhayaraju, C. Hassa, Planar liquid sheet breakup of prefilming and nonprefilming atomizers at elevated pressures, Atomization and Sprays 19 (2009) 1147–1169. doi:10.1615/AtomizSpr.v19.i12.50.
[13] A. K. Jasuja, Behaviour of aero-engine airblast sprays in practical environment, in: Proceedings of the ICLASS, 10th Triennial International Conference on Liquid Atomization and Spray Systems, Aug 27-Sept 1, Kyoto, Japan, 2006.
[14] S. Gepperth, A. Müller, R. Koch, H.-J. Bauer, Ligament and droplet characteristics in prefilming airblast atomization, in: Proceedings of the ICLASS, 12th Triennial International Conference on Liquid Atomization and Spray Systems, September 2-6, Heidelberg, Germany, 2012.

[15] S. Holz, G. Chaussonnet, S. Gepperth, R. Koch, H.-J. Bauer, Comparison of the primary atomization model pamela with drop size distributions of an industrial prefilming airblast nozzle, in: Proceedings of the ILASS Europe, 27th Annual Conference on Liquid Atomization and Spray Systems, September 4-7, Brighton, UK, 2016.
[16] K. Warncke, S. Gepperth, B. Sauer, A. Sadiki, J. Janicka, R. Koch, H.-J. Bauer, Experimental and numerical investigation of the primary breakup of an airblasted liquid sheet, International Journal of Multiphase Flow 91 (2017) 208–224. URL: http://dx.doi.org/10.1016/j.ijmultiphaseflow.2016.12.010. doi:10.1016/j.ijmultiphaseflow.2016.12.010.
[17] C. Bilger, R. Stewart Cant, From high-fidelity numerical simulations of a liquid-film atomization to a regime classification, Atomization and Sprays 28 (2018) 65–89. doi:10.1615/AtomizSpr.2018025001.
[18] C. Bilger, Numerical Investigation of Liquid Film Dynamics and Atomisation in Jet Engine Fuel Injectors, Ph.D. thesis, University of Cambridge, 2018. URL: https://doi.org/10.17863/CAM.21305. doi:10.17863/CAM.21305.
[19] G. Chaussonnet, T. Laroche, C. Lieber, S. Holz, R. Koch, H.-J. Bauer, Investigation of the liquid accumulation characteristics in planar prefilming airblast atomization, in: Proceedings of the ICLASS, 14th Triennial International Conference on Liquid Atomization and Spray Systems, July 22-26, Chicago, IL, USA, 2018.
[20] A. H. Lefebvre, Airblast atomization, Progress in Energy and Combustion Science 6 (1980) 233–261. URL: https://doi.org/10.1016/0360-1285(80)90017-9. doi:10.1016/0360-1285(80)90017-9.
[21] M. M. Aigner, S. Wittig, Swirl and counterswirl effects in prefilming airblast atomizers, Journal of Engineering for Gas Turbines and Power 110 (1988) 105–110. URL: https://doi.org/10.1115/1.3240072. doi:10.1115/1.3240072.
[22] U. C. Bhayaraju, F. Giuliani, C. Hassa, Planar liquid sheet breakup of pre- and nonprefilming airblast atomisers at elevated ambiant air pressures, in: Proceedings of the ILASS Europe, 20th Annual Conference on Liquid Atomization and Spray Systems, September 5-7, Orléans, France, 2005.
[23] J. E. Beck, A. H. Lefebvre, T. R. Koblish, Airblast atomization at conditions of low air velocity, Journal of Propulsion and Power 7 (1991) 207–212. URL: https://doi.org/10.2514/3.23313. doi:10.2514/3.23313.
[24] D. Fuster, J.-P. Matas, S. Marty, S. Popinet, J. Hoepffner, A. Cartellier, S. Zaleski, Instability regimes in the primary breakup region of planar coflowing sheets, Journal of Fluid Mechanics 736 (2013) 150–176. URL: https://doi.org/10.1017/jfm.2013.536. doi:10.1017/jfm.2013.536.
[25] G. Agbaglah, R. Chiodi, O. Desjardins, Numerical simulation of the initial destabilization of an air-blasted liquid layer, Journal of Fluid Mechanics 812 (2017) 1024–1038. URL: https://doi.org/10.1017/jfm.2016.835. doi:10.1017/jfm.2016.835.
[26] T. Inamura, M. Shirota, M. Tsushima, M. Kato, Spray characteristics of prefilming type of airblast atomizer, in: Proceedings of the ICLASS, 12th Triennial International Conference on Liquid Atomization and Spray Systems, September 2-6, Heildelberg, Germany, 2012.
[27] B. Déjan, P. Berthoumieu, P. Gajan, Experimental study on the influence of liquid and air boundary conditions on a planar air-blasted liquid sheet, part i: Liquid and air thicknesses, International Journal of Multiphase Flow 79 (2016) 202–213. URL: https://doi.org/10.1016/j.ijmultiphaseflow.2015.09.002. doi:10.1016/j.ijmultiphaseflow.2015.09.002.
[28] B. Déjan, P. Berthoumieu, P. Gajan, Experimental study on the influence of liquid and air boundary conditions on a planar air-blasted liquid sheet, part ii: prefilming zone length, International Journal of Multiphase Flow 79 (2016) 214–224. URL: https://doi.org/10.1016/j.ijmultiphaseflow.2015.09.001. doi:10.1016/j.ijmultiphaseflow.2015.09.001.
[29] G. Chaussonnet, E. Riber, O. Vermorel, B. Cuenot, S. Gepperth, R. Koch, Large eddy simulation of a prefilming airblast atomizer, in: Proceedings of the ILASS Europe, 25th Annual Conference on Liquid Atomization and Spray Systems, September 1-4, Chania, Greece, 2013.
[30] G. Chaussonnet, O. Vermorel, E. Riber, B. Cuenot, A new phenomenological model to predict drop size distribution in large-eddy simulations of airblast atomizers, International Journal of Multiphase Flow 80 (2016) 29–42. URL: https://doi.org/10.1016/j.ijmultiphaseflow.2015.10.014. doi:10.1016/j.ijmultiphaseflow.2015.10.014.
[31] B. Sauer, A. Sadiki, J. Janicka, Numerical analysis of the primary breakup applying the embedded dns approach to a generic prefilming airblast atomizer, The Journal of Computational Multiphase Flows 6 (2014) 179–192. URL: https://doi.org/10.1260/1757-482X.6.3.179. doi:10.1260/1757-482X.6.3.179.
[32] B. Sauer, A. Sadiki, J. Janicka, Embedded dns concept for simulating the primary breakup of an airblast atomizer, Atomization and Sprays 26 (2016) 187–217. URL: http://dx.doi.org/10.1615/AtomizSpr.2014011019. doi:10.1615/AtomizSpr.2014011019.
[33] B. Sauer, Direct Numerical Simulation of the Primary Breakup of Aircraft Engine Related Two-Phase Flows, Ph.D. thesis, Technische Univesität Darmstadt, 2016.
[34] S. Braun, L. Weith, S. Holz, T. F. Dauch, M. C. Keller, G. Chaussonnet, S. Gepperth, R. Koch, H.-J. Bauer, Numerical prediction of air-assisted primary atomization using smoothed particle hydrodynamics, International Journal of Multiphase Flow (2019).
[35] S. Gepperth, D. Guildenbecher, R. Koch, H.-J. Bauer, Pre-filming primary atomization: Experiments and modeling, in: Proceedings of the ILASS Europe, 23rd Annual Conference on Liquid Atomization and Spray Systems, September 6-8, Brno, Czech Republic, 2010.
[36] A. Müller, Experimentelle Untersuchung des Zerstäubungsverhaltens luftgestützter Brennstoffdüsen bei osczillierenden Strömungen, Ph.D. thesis, Institut für Thermische Strömungsmaschinen (ITS), Karlsruhe Institut für Technologie, 2015.
[37] A. Müller, R. Koch, H.-J. Bauer, M. Hehle, O. Schäfer, Performance of prefilming airblast atomizers in unsteady flow conditions, in: Proceedings of the ASME Turbo Expo 2006: Power for Land, Sea and Air, May 8-11, Barcelona, Spain, 2006. URL: https://doi.org/10.1115/GT2006-90432. doi:10.1115/GT2006-90432.
[38] R. Kapulla, J. Tuchtenhagen, A. Müller, K. Dullenkopf, H.-J. Bauer, Droplet sizing performance of different shadow sizing codes, Gesellschaft für Laser-Anemometrie GALA, Karlsruhe, Germany (2008).
[39] S. J. Kline, F. A. McClintock, Describing uncertainties in single-sample experiments, Mechanical Engineering 75 (1953)

3–8.
[40] T. Mosbach, R. Sadanandan, W. Meier, R. Eggels, Experimental analysis of altitude relight under realistic conditions using laser and high-speed video techniques, in: Proceedings of the ASME Turbo Expo 2010: Power for Land, Sea, and Air, Volume 2: Combustion, Fuels and Emissions, Parts A and B, June 14–18, Glasgow, UK, volume 2, 2010. doi:10.1115/GT2010-22625.
[41] A. Behrendt, T. Nakamura, T. Tsuda, Combined temperature lidar for measurements in the troposphere, stratosphere, and mesosphere, Applied Optics 43 (2004) 2930–2939. URL: http://doi.org/10.1364/AO.43.002930. doi:10.1364/AO.43.002930.
[42] T. Ménard, S. Tanguy, A. Berlemont, Coupling level set/VOF/ghost fluid methods: Validation and application to 3D simulation of the primary break-up of a liquid jet, International Journal of Multiphase Flow 33 (2007) 510–524. URL: https://doi.org/10.1016/j.ijmultiphaseflow.2006.11.001. doi:10.1016/j.ijmultiphaseflow.2006.11.001.
[43] A. Asuri Mukundan, T. Ménard, J. C. Brändle de Motta, A. Berlemont, A 3D Moment of Fluid method for simulating complex turbulent multiphase flows, Computers & Fluids 198 (2020). URL: https://doi.org/10.1016/j.compfluid.2019.104364. doi:10.1016/j.compfluid.2019.104364.
[44] G. Vaudor, T. Ménard, W. Aniszewski, M. Doring, A. Berlemont, A consistent mass and momentum flux computation method for two phase flows. Application to atomization process, Computers & Fluids 152 (2017) 204–216. URL: https://doi.org/10.1016/j.compfluid.2017.04.023. doi:10.1016/j.compfluid.2017.04.023.
[45] B. Duret, G. Luret, J. Réveillon, T. Ménard, A. Berlemont, F.-X. Demoulin, DNS analysis of turbulent mixing in two-phase flows, International Journal of Multiphase Flow 40 (2012) 93–105. URL: https://doi.org/10.1016/j.ijmultiphaseflow.2011.11.014. doi:10.1016/j.ijmultiphaseflow.2011.11.014.
[46] R. Canu, S. Puggelli, M. Essadiki, B. Duret, T. Ménard, M. Massot, J. Réveillon, F. Demoulin, Where does the droplet size distribution come from?, International Journal of Multiphase Flow 107 (2018) 230–245. URL: https://doi.org/10.1016/j.ijmultiphaseflow.2018.06.010. doi:10.1016/j.ijmultiphaseflow.2018.06.010.
[47] V. Chéron, J. C. Brändle de Motta, G. Vaudor, T. Ménard, A. Berlemont, From droplets to particles: Transformation criteria, in: Proceedings of the ILASS Europe, 29th Annual Conference on Liquid Atomization and Spray Systems, September 2-4, Paris, France, 2019.
[48] J. Cousin, T. Ménard, A. Berlemont, S. Grout, Primary breakup simulation of a liquid jet discharged by a low-pressure compound nozzle, Computers & Fluids 63 (2012) 165–173. URL: http://dx.doi.org/10.1016/j.compfluid.2012.04.013. doi:10.1016/j.compfluid.2012.04.013.
[49] B. Duret, J. Réveillon, T. Ménard, F. X. Demoulin, Improving primary atomization modeling through DNS of two-phase flows, International Journal of Multiphase Flow 55 (2013) 130–137. URL: https://doi.org/10.1016/j.ijmultiphaseflow.2013.05.004. doi:10.1016/j.ijmultiphaseflow.2013.05.004.
[50] A. Asuri Mukundan, G. Tretola, T. Ménard, M. Herrmann, S. Navarro-Martinez, K. Vogiatzaki, J. C. Brändle de Motta, A. Berlemont, DNS and LES of primary atomization of turbulent liquid jet injection into a gaseous crossflow environment (2020). URL: https://doi.org/10.1016/j.proci.2020.08.004. doi:10.1016/j.proci.2020.08.004.
[51] M. Sussman, K. M. Smith, M. Y. Hussaini, M. Ohta, R. Zhi-Wei, A sharp interface method for incompressible two-phase flows, Journal of Computational Physics 221 (2007) 469–505. URL: https://doi.org/10.1016/j.jcp.2006.06.020. doi:10.1016/j.jcp.2006.06.020.
[52] R. Fedkiw, T. Aslam, B. Merriman, S. Osher, A Non-oscillatory Eulerian Approach to Interfaces in Multimaterial Flows (the Ghost Fluid Method), Journal of Computational Physics 152 (1999) 457–492. URL: https://doi.org/10.1006/jcph.1999.6236. doi:10.1006/jcph.1999.6236.
[53] S. Tanguy, A. Berlemont, Application of a level set method for simulation of droplet collisions, International Journal of Multiphase Flow 31 (2005) 1015–1035. URL: https://10.1016/j.ijmultiphaseflow.2005.05.010. doi:10.1016/j.ijmultiphaseflow.2005.05.010.
[54] T.-T. Vu, Atomization process of turbulent liquid sheets. Experimental analyses & numerical developments, Ph.D. thesis, Université de Rouen Normandie, 2017. URL: http://www.coria.fr/spip.php?article1105&titre_mot=these.
[55] M. Klein, A. Sadiki, J. Janicka, A digital filter based generation of inflow data for spatially developing direct numerical or large eddy simulations, Journal of Computational Physics 186 (2003) 652–665. URL: https://doi.org/10.1016/S0021-9991(03)00090-1. doi:10.1016/S0021-9991(03)00090-1.
[56] S. B. Pope, Turbulent Flows, Cambridge University Press, 2000.
[57] M. Gorokhovski, M. Herrmann, Modeling primary atomization, Annual Review of Fluid Mechanics 40 (2008) 343–366. URL: https://doi.org/10.1146/annurev.fluid.40.111406.102200. doi:10.1146/annurev.fluid.40.111406.102200.
[58] Utilisation du Cluster Myria, CRIANN Supercomputing Facility, Centre Régional Informatique et d'Applications Numériques de Normandie, 2018. URL: http://www-tech.criann.fr/calcul/tech/myria-doc/guide-util/.
[59] A. Asuri Mukundan, T. Ménard, A. Berlemont, J. C. Brändle de Motta, Coupled Level set moment of fluid method for simulating multiphase flows, in: Proceedings of the ILASS Europe, 29th Annual Conference on Liquid Atomization and Spray Systems, September 2-4, Paris, France, 2019. URL: https://hal.archives-ouvertes.fr/hal-02318029/document.
[60] V. Dyadechko, M. Shashkov, Reconstruction of multi-material interfaces from moment data, Journal of Computational Physics 227 (2008) 5361–5384. URL: https://doi.org/10.1016/j.jcp.2007.12.029. doi:10.1016/j.jcp.2007.12.029.
[61] M. Jemison, E. Loch, M. Sussman, M. Shashkov, M. Arienti, M. Ohta, Y. Wang, A Coupled Level Set-Moment of Fluid Method for Incompressible Two-Phase Flows, Journal of Scientific Computing 54 (2013) 454–491. URL: https://doi.org/10.1007/s10915-012-9614-7. doi:10.1007/s10915-012-9614-7.
[62] D. Gueyffier, A. Nadim, R. Scardovelli, S. Zaleski, Volume-of-Fluid Interface Tracking with Smoothed Surface Stress Methods for Three-Dimensional Flows, Journal of Computational Physics 152 (1999) 423–456. URL: https://doi.org/10.1006/jcph.1998.6168. doi:10.1006/jcph.1998.6168.

[63] G. D. Weymouth, D. K.-P. Yue, Conservative Volume-of-Fluid method for free-surface simulations on Cartesian-grids, Journal of Computational Physics 229 (2010) 2853–2865. URL: https://doi.org/10.1016/j.jcp.2009.12.018. doi:10.1016/j.jcp.2009.12.018.

[64] M. Sussman, E. G. Puckett, A Coupled Level Set and Volume-of-Fluid Method for Computing 3D and Axisymmetric Incompressible Two-Phase Flows, Journal of Computational Physics 162, (2000) 301–337. URL: https://doi.org/10.1006/jcph.2000.6537. doi:10.1006/jcph.2000.6537.

[65] A. Asuri Mukundan, Numerical development of Moment of Fluid/Level Set method and Application to liquid jet and sheet atomization, Ph.D. thesis, Université de Rouen Normandie, 2020.

[66] V. G. Fernández, P. Berthoumieu, G. Lavergne, Liquid sheet disintegration at high pressure: An experimental approach, Comptes Rendus Mécanique 337 (2009) 481–491. URL: https://doi.org/10.1016/j.crme.2009.06.026. doi:10.1016/j.crme.2009.06.026.

[67] M. Behzad, A. Mashayek, N. Ashgriz, A KIVA-based model for liquid jet in crossflow, in: Proceedings of the ILASS Americas, 22nd Annual Conference on Liquid Atomization and Spray Systems, May 16-19, Cincinnati, OH, USA, ILASS2010-112, 2010.

[68] M. Herrmann, A parallel Eulerian interface tracking/Lagrangian point particle multi-scale coupling procedure, Journal of Computational Physics 229 (2010) 745–759.

[69] M. Pilch, C. A. Erdman, Use of breakup time data and velocity history data to predict the maximum size of stable fragments for acceleration-induced breakup of a liquid drop, International Journal of Multiphase Flow 13 (1987) 741–757. URL: https://doi.org/10.1016/0301-9322(87)90063-2. doi:10.1016/0301-9322(87)90063-2.

[70] A. Asuri Mukundan, T. Ménard, A. Berlemont, J. C. Brändle de Motta, An investigation of characteristics of airblast atomization using 3D DNS for altitude relight conditions, in: 11th U.S. National Combustion Meeting, April 24-27, Pasadena, California, USA, 2019. URL: https://hal.archives-ouvertes.fr/hal-02092003/document.

[71] A. Asuri Mukundan, T. Ménard, A. Berlemont, J. C. Brändle de Motta, R. Eggels, Validation and Analysis of 3D DNS of planar pre-filming airblast atomization simulations, in: Proceedings of the ILASS Americas, 30th Annual Conference on Liquid Atomization and Spray Systems, May 12-15, Phoenix, AZ, USA, 2019. URL: https://hal.archives-ouvertes.fr/hal-02178046/document.

[72] A. Asuri Mukundan, T. Ménard, A. Berlemont, J. C. Brändle de Motta, A comparative study of DNS of airblast atomization using CLSMOF and CLSVOF methods, in: Proceedings of the ILASS Europe, 29th Annual Conference on Liquid Atomization and Spray Systems, September 2-4, Paris, France, 2019. URL: https://hal.archives-ouvertes.fr/hal-02318020/document.

[73] N. Fdida, J.-B. Blaisot, Morphological characterization of droplets. application to atomization of sprays, in: ISFV13-13th International Symposium on Flow Visualization, FLUVISU12 - 12th French Congress on Visualization in Fluid Mechanics July 1-4, Nice, France, 2008.

[74] J.-B. Blaisot, Analysis of backlight images for spray measurement: how to accurately identify the liquid-gas interface in images, in: Proceedings of the ICLASS, 14th Triennial International Conference on Liquid Atomization and Spray Systems, July 22-26, Chicago, IL, USA, 2018.